PNNL-15947

Pacific Northwest
National Laboratory
Operated by Battelle for the
U.S. Department of Energy

Corrosion of Metal Inclusions In Bulk Vitrification Waste Packages

D. H. Bacon
E. M. Pierce
D. M. Wellman
D. M. Strachan
G. B. Josephson

July 2006

Prepared for the U.S. Department of Energy
under Contract DE-AC05-76RL01830

DISCLAIMER

PACIFIC NORTHWEST NATIONAL LABORATORY
operated by
BATTELLE
for the
UNITED STATES DEPARTMENT OF ENERGY
under Contract DE-AC05-76RL01830

Printed in the United States of America

Available to DOE and DOE contractors from the
Office of Scientific and Technical Information,
P.O. Box 62, Oak Ridge, TN 37831-0062;
ph: (865) 576-8401
fax: (865) 576-5728
email: reports@adonis.osti.gov

Available to the public from the National Technical Information Service,
U.S. Department of Commerce, 5285 Port Royal Rd., Springfield, VA 22161
ph: (800) 553-6847
fax: (703) 605-6900
email: orders@ntis.fedworld.gov
online ordering: http://www.ntis.gov/ordering.htm

This document was printed on recycled paper.
(2/01)

PNNL-15947

Corrosion of Metal Inclusions in Bulk Vitrification Waste Packages

D. H. Bacon
E. M. Pierce
D. M. Wellman
D. M. Strachan
G. B. Josephson

July 2006

Prepared for
the U.S. Department of Energy
under Contract DE-AC05-76RL01830

Pacific Northwest National Laboratory
Richland, Washington 99352

Summary

The primary purpose of the work reported here is to analyze the potential effect of the release of technetium (Tc) from metal inclusions in bulk vitrification (BV) waste packages once they are placed in the Integrated Disposal Facility (IDF). As part of the strategy for immobilizing waste from the underground tanks at Hanford, selected wastes will be immobilized using BV. During analyses of the glass produced in engineering-scale tests, metal inclusions were found in the glass product. This report contains the results from experiments designed to quantify the corrosion rates of metal inclusions found in the glass product from Test ES-32B (AMEC 2005) and simulations designed to compare the rate of Tc release from the metal inclusions to the release of Tc from glass produced with the BV process. Due to the probability of oxidizing conditions surrounding the waste packages in the IDF, in the simulations the Tc in the metal inclusions and the glass is conservatively assumed to be released congruently as soluble TcO_4^-. The experimental results and modeling calculations (Bacon and McGrail 2005) show that the metal corrosion rate will, under all conceivable conditions at the IDF, be dominated by the presence of the passivating layer and corrosion products on the metal particles. As a result, the release of Tc from the metal particles at the surfaces of fractures in the glass releases at a rate similar to the Tc present as a soluble salt (McGrail et al. 2003; Pierce et al. 2005). The release of the remaining Tc in the metal is controlled by the dissolution of the glass matrix.

The dissolution kinetics of iron [Fe(0)] was quantified under conditions of constant dissolved O_2 [O_2 (aq)] and in solutions that minimized the formation of a passive film on the metal surface. These tests were performed to determine the forward reaction rate for the metal inclusions in the BV glass. Single-pass flow through (SPFT) tests were conducted over the pH(23°C) range from 7.0 to 12.0 and temperature range from 23°C to 90°C. The presence of EDTA minimized the formation of a passive film and Fe-bearing secondary phase(s) during testing allowing us to determine the forward dissolution rate. These results indicate that the corrosion of Fe(0) is relatively insensitive to pH and temperature and the forward rate is 3 to 4 orders of magnitude higher than when a passive film and corrosion products are present. Tests conducted with Amasteel (a low carbon steel non-radioactive surrogate) and ES-32B metal indicated that the forward dissolution rates for both metals were similar, if not identical. In other words, the presence of P and ^{99}Tc in the ES-32B metal appeared to have little effect on the forward dissolution rate. These results indicate that the corrosion rate of the ES-32B metal at repository relevant conditions was not significantly less than the surrogate metal. Because the effects of temperature (E_a = 15 ±5 kJ/mol at pH(23°C) = 9.0 based on Fe release from ES-32B metal) and solution pH (η = -0.13 ±0.02 at 70°C based on Fe release from ES-32B metal) were determined to be relatively small under these test conditions, we were unable to obtain reliable rate-law parameters for the metal. Because of the difficulty in obtaining the forward dissolution rate, we conclude that under all conceivable conditions at the IDF a passive film and iron corrosion products will be present and they will control metal inclusion dissolution rates. Thus, for the PA

calculations presented here, a field-measured corrosion rate for low-carbon steel of 0.2 mil/y (0.11 g/(m^2·d)) was used for the maximum corrosion rate for the metals incorporated in the BV product.

A range of field-measured rates were used to simulate release rates of ^{99}Tc from metal inclusions in BV waste packages emplaced in the IDF. The results of these simulations indicate that ^{99}Tc release rates from metal inclusions are likely to be two to four orders of magnitude higher than release rates of ^{99}Tc from the glass itself, during the first 2000 years after waste packages have been breached. However, the release rates of Tc to the groundwater are insensitive to the corrosion rates assumed for the metal inclusions, because the corrosion rates are fast relative to travel times through the vadose zone. Technetium release rates from BV product with metal inclusions are sensitive to the size assumed for the inclusions because the larger the radius of the metal inclusions, the more likely inclusions are to be exposed by a fracture in the glass. Based on the modeling studies, peak ^{99}Tc release rates from the metal inclusions are linearly proportional to the amount of metal in the glass waste packages, whereas long-term ^{99}Tc release rates from the metal inclusions are limited by the corrosion rate of glass. Elevated Tc concentrations due to glass corrosion may inhibit iron corrosion for 500 years, thus delaying the release of Tc from the metal. However, delaying the release of Tc in the metal by 500 years is unlikely to have a significant impact on final groundwater concentrations.

To summarize, the release of ^{99}Tc from the BV glass within precipitated Fe is directly proportional to the diameter of the Fe particles and to the amount of precipitated Fe. However, the main contribution to the Tc release from the iron particles is over the same time period as the release of the soluble Tc salt. For the base case used in this study (0.48 mass% of 0.5 mm diameter metal particles homogeneously distributed in the BV glass), the release of ^{99}Tc from the metal is approximately the same as the release from 0.3 mass% soluble Tc salt in the castable refractory block and it is released over the same time period as the salt. Therefore, to limit the impact of precipitated Fe on the release of ^{99}Tc, both the amount of precipitated Fe in the BV glass and the diameter of these particles should be minimized.

Contents

Figures

Tables

1.0 Introduction

The Hanford Site in southeastern Washington State is managed by the U.S. Department of Energy (DOE) and has been used extensively to produce nuclear materials for the U.S. strategic defense arsenal. A large inventory of radioactive and mixed waste has accumulated in 177 single-shell and double-shell tanks. Waste recovered from the tanks will be pre-treated to separate the low-activity fraction from the high-level and transuranic fraction of the waste. The volume of the low-activity fraction will be among the largest in the DOE complex and contains one of the largest inventories of long-lived radionuclides, principally ^{99}Tc, planned for disposal in a low-level waste facility. Currently, the DOE Office of River Protection (ORP) is evaluating several options for immobilizing low-activity tank wastes for eventual disposal in a shallow subsurface facility, the Integrated Disposal Facility (IDF), at the Hanford Site (Puigh 2004). A significant portion of the waste will be converted into immobilized low-activity waste (ILAW) glass with a conventional Joule-heated ceramic melter. In addition to ILAW glass, DOE is considering a supplemental treatment technology, bulk vitrification (BV), to treat a portion of the low-activity waste (LAW). The use of a supplemental treatment technology could accelerate the overall cleanup mission at the Hanford site by as much as 35 years.

Before the ILAW and BV can be disposed in the IDF, DOE must approve (DOE O 435.1) a performance assessment (PA), which is a document that describes the long-term impacts of the disposal facility on public health and environmental resources. A sound scientific basis for determining the long-term release rates of radionuclides from LAW glasses must be developed if the PA is to be accepted by regulatory agencies, stakeholders, and the public, in accord with the Tri-Party Agreement. A critical component of the PA provides quantitative estimates of radionuclide release rates from the engineered portion of the disposal facilities (source term). Computer models are essential for this purpose because effects on groundwater resources must be projected to 10,000 years after IDF closure. Details on the recommended technical strategy for developing this source term have been published (McGrail et al. 2003) and have undergone review by an international panel of experts.

To estimate the waste form release rates for these PAs, Pacific Northwest National Laboratory (PNNL) has contributed waste form release simulations (Chen et al. 1997; Bacon and McGrail 1998; Bacon and McGrail 2001; Bacon et al. 2002; Bacon and McGrail 2003; Bacon and McGrail 2005) that are based on data packages quantifying dissolution rates of waste package materials, including ILAW and BV glasses (Mann et al. 2001; Pierce et al. 2004a; Pierce et al. 2004b). The waste form release simulations are performed with the Subsurface Transport Over Reactive Multiphases (STORM) code (Bacon et al. 2004). With the STORM code, one has the capability to simulate the special glass kinetic reaction, in which many aqueous species are released. However, equilibrium depends only on a few of the aqueous species, such as dissolved silica and alumina. Also, reactive transport in STORM is fully coupled with unsaturated flow; the unsaturated flow field may be altered by dissolution and precipitation of minerals.

During engineering-scale testing of the BV process, large blocks of glass product, both radioactive and radioinactive, were examined to determine the fate of the ^{99}Tc or the stand-in element Re in these glasses. In these examinations, inclusions of iron metal were found. This iron was in the form of a large slab in one test product and as small spherically shaped particles in others. A substantial amount of ^{99}Tc or Re was present in these metal inclusions. Like the Tc in the soluble salts that accumulate on the surface of the BV product, there was a concern that the presence of ^{99}Tc in the metal inclusions and the rapid corrosion of these inclusions could substantially add to the release rate of ^{99}Tc to the groundwater. Therefore, the primary purpose of work reported here is to analyze the potential effect of metal inclusions on the release of ^{99}Tc from BV waste packages once they are placed in the IDF. This report contains the results of experiments designed to quantify the corrosion rates of metal inclusions from Test ES-32B[1] (AMEC 2005). These experimental results were incorporated into PA simulations recently conducted for BV waste packages (Bacon and McGrail 2005), which were based on experimental data quantifying the corrosion rates of BV glass (Pierce et al. 2004b).

1.1 Theoretical Considerations

The geochemical cycling of iron has been the subject of studies for several decades. For additional details on the cycling of Fe and the influence of Fe on environmental systems, see Schwertmann and Taylor (1977) and Stumm and Sulzberger (1992). In general, the majority of this work has been focused on the weathering of ferric oxides and hydroxides (e.g., goethite [α-FeOOH], hematite [Fe_2O_3], and lepidocrocite [γ-FeOOH]) and their role in influencing the geochemical cycles of P, S, heavy metals, O_2, and C in the environment (Stumm and Sulzberger 1992; Bruno et al. 1992; Zutic and Stumm 1984). Unlike the afore mentioned Fe-bearing minerals, zero-valent iron [Fe(0)] does not occur naturally and requires extreme anoxic reducing conditions to form, therefore it is environmentally unstable relative to oxidized Fe as oxide or more complex mineral phases (Figure 1-1). As indicated in this

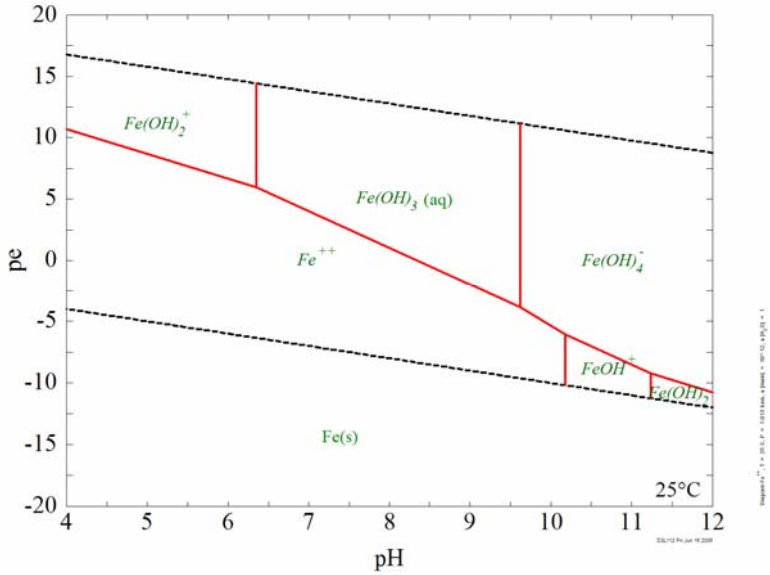

Figure 1-1. Eh-pH diagram of the Fe-H_2O system: $\log_{10}[Fe]_T$ = -12, P = 101 kPa, and a_{H2O} = 1.0. The dashed lines represent the upper and lower stability limits for water.

[1] An earlier numbering system also referred to the ES-32B test as ES-13; ES-32B is used through out this document.

figure, Fe metal lies below the water stability line, the lower dashed line in Figure 1-1, meaning that at all pH values Fe will reduce water to hydroxide and H_2 gas. Fortunately, this water reduction reaction is slow and kinetically unfavorable in most environmental systems because of the presence of other oxidizing agents. Because Fe(0) has a high reductive capacity, researchers have begun using it to treat groundwater contaminated with redox-sensitive heavy metals, radionuclides, and organics, such as trichloroethene (TCE) (Yabusaki et al. 2001), nitro aromatic compounds (Klausen et al. 2003), Cr(VI) (Fruchter 2002), U(VI) (Gu et al. 1998; Abdelouas et al. 1999), and Tc(VII) (Cantrell et al. 1995). These experiments provide some information on the chemical reactions that occur during the corrosion of Fe(0). Additional information, focused on the corrosion of steel, is available in the electrochemical literature.

The dissolution of Fe(0) is believed to be a surface controlled process similar to the oxidative and/or reductive dissolution of ferrous and ferric oxides (Zinder et al. 1986; Sulzberger et al. 1989). In general, the oxidative-dissolution of Fe is thought to occur via the following steps: (1) adsorption of an oxidizing species (in this case dissolved O_2), (2) surface coordination, (3) oxidation of Fe(0) to Fe(II), and (4) detachment of the oxidized species (Stumm 1992). It has also been suggested that in the presence of water and dissolved oxygen, the oxidative-dissolution of Fe(0) may involve reactive oxygen intermediates, such as hydrogen peroxide (H_2O_2), superoxide radical ($O_2^{\bullet-}$), and hydroxide radical (•OH). The formation of these intermediates is postulated to be continuous by the reduction of dissolved O_2, a reaction that can take place either on the Fe(0) surface or in solution, see Noradoun and Cheng (2005) and the references contained therein. Studies with ferrous oxides suggest that detachment of the oxidized species is the rate-limiting step in the dissolution process. The mixed Fe(II) and Fe(III) oxides result in the formation of a passive film (i.e., partially oxidized surface film), typically a few nanometers thick. The mechanism of dissolution and the composition of this passive film is complex and the composition seems to vary from Fe_3O_4 (magnetite), in oxygen free solutions, to $Fe_{2.67}O_4$ in the presence of oxygen (Stumm 1990). The passive film is a three-dimensional oxide layer that protects the Fe(0) surface from corrosion (Davenport et al. 2000). Results from a more detailed investigation with a pH 8.4 borate buffer solution suggest the passive film is a bilayer structure that is composed of an inner layer of defect Fe_3O_4 (probably magnetite) and an outer layer of γ-Fe_2O_3 (probably maghemite) (Büchler et al. 1997). Currently, it is believed that the outer layer, which significantly modifies the electrochemical response of Fe(0) at the solid-solution interface, forms by precipitation; whereas the inner layer is an actual barrier layer that is involved in the passivation of iron (Lui and Macdonald 2001). Thus, the resistance of Fe(0) to corrosion is determined by the stability of the passive film (Davenport et al. 2000). For example, the mechanism of reductive dissolution of the oxidized layer, which causes the breakdown of the passive layer, has been shown to be associated with valence changes within the film (Davenport et al. 2000). Therefore, an effective passive film will resist breakdown, a process that can lead to different forms of localized corrosion, (e.g., pit and crevice corrosion).

Although the processes discussed above represent a large amount of research on the corrosion of Fe(0), few results are available that quantify the rate value required to conduct long-term PA

calculations. Therefore, the purpose of the single-pass flow-through (SPFT) tests discussed in this report was to determine the dissolution kinetics of Fe(0) in the presence of atmospheric oxygen as a function of temperature, solution saturation state, and pH. Accordingly, the principal objective was to determine a representative rate that can be used in the STORM code to model the long-term corrosion of Fe(0) metal inclusions produced as a result of a reduction reaction during the bulk vitrification (BV) process and release of ^{99}Tc from the metal. Although the thermodynamic stability of Fe(0) with respect to water and corrosion products is well known, the kinetics by which Fe(0) dissolves is largely unknown for the disposal situation in which there is flow of water across the metal surface. By examining the dissolution of Fe(0) over a large flow-rate to sample-surface area interval, we were able to quantify some of the kinetic parameters for the dissolution Fe(0).

2.0 Quality Assurance

The work described in this report was performed under the PNNL Nuclear Quality Assurance Requirements Description (NQARD) procedures in accordance with the Supplemental Treatment Technologies Support Program, Tank Waste Support Quality Assurance Plan Rev. 7. These project quality assurance procedures and the project QA plan are compliant with the national standard ASME/NQA-1 as required in the project sponsor's statement of work. Testing documented in this report was performed in accordance with the Test Plan: "Durability Measurements on Metal Inclusions Found in Bulk Vitrified Glass Using the Single-Pass Flow-Through (SPFT) Test Method" 46611-2005-01, Rev.0.

Development of the STORM code was conducted in accordance with "Tank Waste Support Quality Assurance Plan, Supplemental Technologies Support Program" and the applicable NQARD procedures for software control and management of data. Records of model development, testing, and application are stored in project records. The verification studies for STORM are documented in the STORM user's guide (Bacon et al. 2004).

3.0 Iron Corrosion

3.1 Field Measurements

Iron inclusions were observed in the ES-32B test of the BV process and were found to incorporate a significant amount of the Tc or Re in the original feed to the process. These metal inclusions could form in other BV products and, for corrosion purposes, can be considered as low alloy steels and carbon steels (Cartledge 1963). Significant literature is available on the corrosion of low alloy steels and steel in soils (see the discussion above for example). Overall steel corrosion rates in disturbed soils range from 3 μm/y (0.1 mils/y) to 63 μm/y (2.5 mils/y) with an average of about 20 μm/y (0.8 mils/y) (Matsushima 2000) or a dissolution rate of 0.4 g/(m^2·d).

The major factors governing the corrosion of a metal in a given soil are porosity (aeration), electrical conductivity, moisture of the soil and the dissolved salts, and the acidity or alkalinity of the pore water in the soil. The relationships between these factors are complex such that an increase in one factor may increase corrosion under one condition, but reduce corrosion when other factors are changed. No single factor controls the overall corrosion rate. The ranges cited in Matsushima (2000) were determined from a 12-year study carried out at the National Institute of Standards and Technology on buried pipes at 44 locations throughout the United States (Matsushima 2000). The highest metal corrosion rates were for moderately well-drained soils with low electrical resistance and moderately low air content. The lowest corrosion rates were for metals in well-drained soils with high aeration and high electrical resistance; conditions similar to those for Hanford soils.

Several studies of the mild steel corrosion in Hanford soils have been conducted since the early 1950s in conjunction with the corrosion of underground tanks and buried drums of waste. Among the more recent and relevant are corrosion studies of buried steel drums. In 1994, drums of low-level waste that had been buried between 14 and 15 years were exhumed and visually examined. The thickness of the remaining metal was measured ultrasonically and compared to the thickness specifications for new drums (Duncan et al. 1995). More than 90 drums were examined to arrive at estimated corrosion rates. It was found that one drum was breached, but all other drums displayed corrosion rates <25 μm/y (<1 mil/y) and most were <13 μm/y (<0.5 mils/y), approximately at the lower corrosion rate cited by Matsushima (2000).

Corrosion rates of several metal alloys were determined in Hanford soils by burying weighed coupons for periods of 6, 9, and 12 months (Duncan and Bunnell 1995), and at depths of 3, 6, and 9 m (10, 20, and 30 feet). Although each depth had different moisture and temperature conditions, the soil type was the same at all depths. Low carbon steel coupons buried for one year displayed corrosion rates between 4.8 μm/y (0.19 mil/y) at 9-m depth and 25 μm/y (1 mil/y) at 3-m depth. Corrosion rates at 6-m depth were between the rates at 3 and 9 m. Coupons buried for 6 and 9 months displayed higher corrosion rates when normalized to a yearly rate indicating

that corrosion is high initially and decreases with time. An average corrosion rate over a long period, representative of long-term release from a waste disposal site, will likely be even lower than the measured rate for one year.

The corrosion rates from all sources discussed in this section are summarized in Table 3-1.

Table 3-1. Corrosion Rates of Iron/Steel in Soil

Source	High Rate mil/y (µm/y)	Low Rate mil/y (µm/y)	"Average" Rate mil/y (µm/y)	"Average" Rate g/(m^2·d)[a]
U.S. averages (Matsushima 2000)	2.5 (64)	0.1 (2.5)	0.8 (20)	0.38
Hanford buried drums (Duncan et al. 1995)	2 (50)	0.2 (5)	<0.5 (12)	0.24
Hanford buried coupons (Duncan and Bunnell 1995)	1.0 (25)	0.2 (5)	0.6 (15)	0.29

a – Based on a density of $7 \cdot 10^3$ kg/m^3 to give the reader some context with respect to the reporting values for dissolution rates

Work by Cartledge at Oak Ridge National Laboratory from the late 1950s to early 1970s suggests that Tc reduces the corrosion of steels (Cartledge 1963; Cartledge 1966; Cartledge 1962; Cartledge 1973). Cartledge studied the effects of pertechnetate ion in water contacting iron and discovered that concentrations of pertechnetate as low as 5 ppm in the water essentially stopped corrosion on iron (Cartledge 1963; Cartledge 1966; Cartledge 1962; Cartledge 1973). Cartledge showed that Tc (as pertechnetate [TcO_4^-]) was much more powerful at reducing corrosion than Cr (as chromate). The mechanism for the corrosion resistance is not fully understood, but Cartledge suggested that some Tc was adsorbed onto the surface of the iron and was not readily removed. Cartledge (1973) estimated the amount of "bound" Tc to be less than a monolayer, ~2.2×10^{12} atoms/mm^2.

Regarding the ability of Tc to render iron/steel corrosion resistant, the most critical experiment showed that if the TcO_4^- was completely removed from the contacting water, then the corrosion resistance also disappeared (Cartledge 1963; Cartledge 1973). This would mean that if iron containing Tc were in contact continuously with fresh water such that no TcO_4^- accumulated in the aqueous phase, then the iron would corrode at rates similar to iron without Tc. On the other hand, if the water volume contacting the iron was limited so that TcO_4^- could accumulate in the water, then the iron corrosion rate was similar to that in a solution containing 5 ppm TcO_4^-. As the TcO_4^- approached 5 ppm, the iron corrosion rate and concomitant release of Tc decreased nearly to zero. This established an upper limit on the TcO_4^- concentration in water directly contacting iron.

3.2 Laboratory Measurements

A critical component of the PA is providing quantitative estimates of radionuclide release rates from the engineered portion of the disposal facilities (source term). In FY 2003 and FY 2004, tests on several representative BV glasses were conducted to determine the kinetic rate law

parameters (McGrail et al. 2003; Pierce et al. 2005). Although the kinetic rate data measured for the BV glasses tested to-date have been comparable to Waste Treatment Plant (WTP) glasses, the formation of metal inclusions in the BV product has resulted in the need to assess the effect of these inclusions on the long-term performance of the BV waste package, in particular the overall release of Tc to the groundwater.

A scanning electron microscope (SEM) image of a BV sample removed from ES-32B that contained a metal inclusion is shown in Figure 3-1. This image illustrates a distinctive glass/metal interface where the metal has precipitated as a separate phase. An X-ray diffraction (XRD) analysis of a metal inclusion removed from LS-38A gave the diffraction pattern shown in Figure 3-2 that could be indexed as α-Fe. Chemical analyses of the ES-32B sample indicated that the iron was composed of Fe (93.5 mass%) and P (5.8 mass%) with several other minor components (Table 3-2). Figure 3-2 also shows the presence in the diffraction pattern of a few weak reflections that are associated with a minor phase that has not been identified. The metal samples removed from LS-38A and ES-32B have similar compositions. Relevant to the PA calculations is the fact that the Fe contains approximately 0.01 mass% ^{99}Tc (Table 3-2).

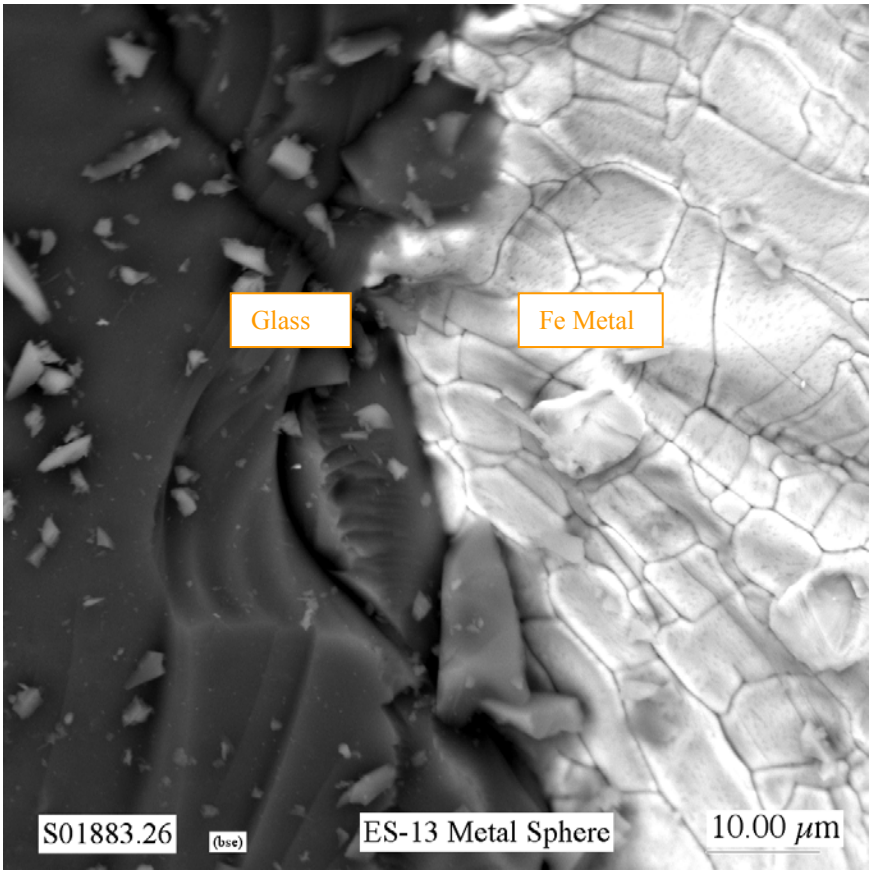

Figure 3-1. An SEM image of Metal Inclusions (right side of image) Contained in the BV Glass (left side of image). Sample Removed from ES-32B Test.

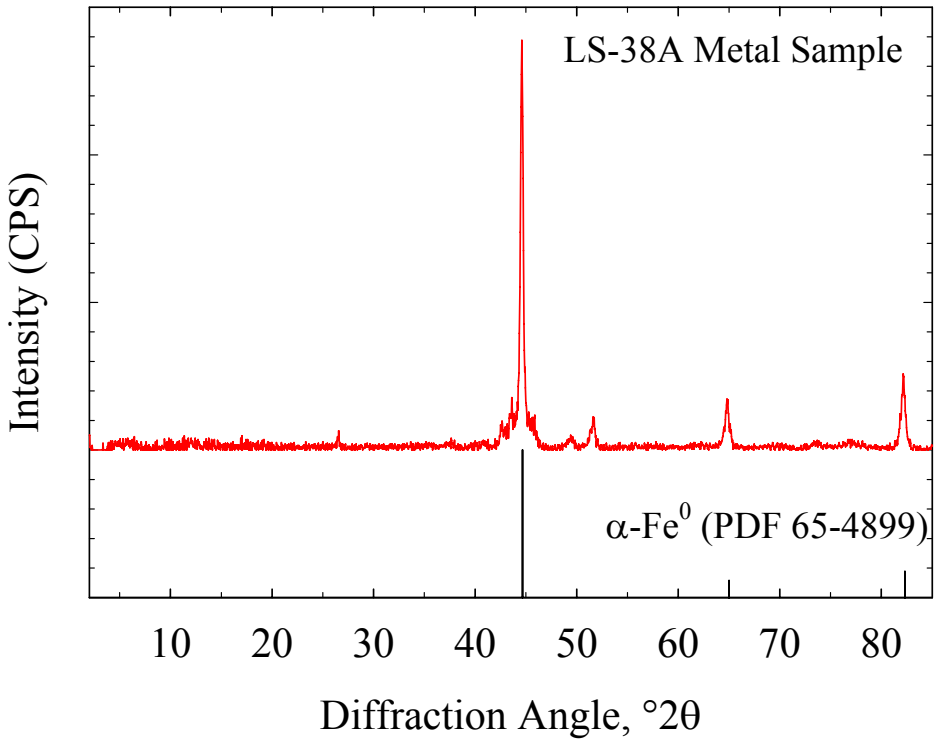

Figure 3-2. An XRD Pattern of a Metal Inclusions Sample Contained in the BV Glass Taken from LS-38A. (PDF = powder diffraction file of XRD patterns.)

Based in part on the chemical analysis of the metal found in the ES-32B test product and the availability of an iron powder that was obtained through another project, we also characterized some Amasteel iron powder that was produced at Ervin Technologies (Tecumseh, MI) with a gas atomization process. The rapidly cooled metal droplets form well defined nearly spherical particles (Figure 3-3). This metal powder was used as the non-radioactive surrogate for the ES-32B metal inclusions and allowed us to perform a variety of tests to determine kinetic parameters. These tests would not have been possible if we were to use just the metal inclusions from the ES-32B test product. The composition of both metals is shown in Table 3-2.

Table 3-2. Composition of ES-32B Metal Inclusion and Commercially Available α-Fe in Mass%.

Component	aBV-ES13-T-G-22 (ES-32B)	Amasteel b
Al	0.03	
As	0.01	
C		0.01
Ca	0.01	
Cr	0.01	0.13
Co	0.05	
Cu	0.06	0.22
Fe	93.46	99.2
Mn		0.10
Mo	0.01	0.08
Ni	0.09	0.12
P	5.75	0.022
Pb		0.012
K	0.01	
Si	0.01	0.09
Na	0.09	
Re	0.01	
S	0.35	0.025
Sn	0.02	
^{99}Tc	0.01	
W	0.01	

aNormalized to 100%.
bReceived from Ervin Technologies.

Although these samples both contain > 90% Fe, the large amount of P and ^{99}Tc contained in the ES-32B sample may play a significant role in the overall corrosion behavior of this metal. For example, the slow corrosion of the Delhi iron pillar has, in part, been attributed to the presence of a significant concentration of phosphorous (Balasubramaniam 2000). Therefore, SPFT experiments with the metal powder from Ervin Technologies should yield corrosion rates that are upper bounds to the rates obtained from experiments with the ES-32B metal.

3.2.1 Material Preparation and Surface Area Determination

Conditioned Amasteel was received from Ervin Technologies and sieved into the 425 to 250 μm (-40 +60 mesh) size fraction with standard American Society of Testing and Materials (ASTM) sieves (ASTM 2001). Although the ES-32B metal was sized in a similar fashion, the metal first

had to be crushed in a ceramic ball mill. After screening, both samples of metal were washed, washed again in an ultrasonic bath, rinsed in ethanol, and dried in a 90°C (±2°C) oven.

An estimate of the geometric surface area was determined with the geometric equation McGrail et al. (1992; 1997), Equation (1),

$$S_{GEO} = \frac{3}{\rho r} \tag{1}$$

where S_{GEO} = specific surface area in m^2/g, r = is the average radius of the particle (m), and ρ = is the particle density (kg/m^3). The particle density of the Fe metal, measured with an Accupyc 1330 He pycnometer (Micromeritics, Norcross, GA), was determined to be (7.703 ±0.001) × 10^3 kg/m^3 for Amasteel and (6.73 ±0.02) × 10^3 kg /m^3 for the ES-32B metal particle or specific surface areas of 1.15 m^2/g and 1.32 m^2/g, respectively. In Equation (1) the grains are assumed to be spherical and the sizes are normally distributed; surface pits, cracks, and other forms of surface roughness do not affect the surface area. The Amasteel particles are nearly spherical and the sizes appear to be normally distributed, as evident from the SEM images of the pre- (Figure 3-3) and post-test grains. These results suggest that, in the case of the Amasteel, two of the three assumptions used to determine the geometric surface area are satisfied. Although this assumption may not be entirely valid for the ES-32B metal because of their irregular shaped particles, for the purpose of consistency all rates reported in this study were calculated with the calculated geometric surface area. Another factor that complicates the estimate of specific surface area is the change each sample undergoes over the duration of the dissolution experiment. Therefore, the equations developed by McGrail et al. (1997), which allow for the change in sample mass over the duration of the experiment to be computed, were used to compensate for this effect. The background corrected iron concentration for the Amasteel and ^{99}Tc concentration for the ES-32B metal contained in the effluent solution sample was used to calculate the change in sample mass. In the case of ES-32B metal, we used ^{99}Tc as the indicator of corrosion with the assumption that once contacted by water it is oxidized to TcO_4^- and does not precipitate.

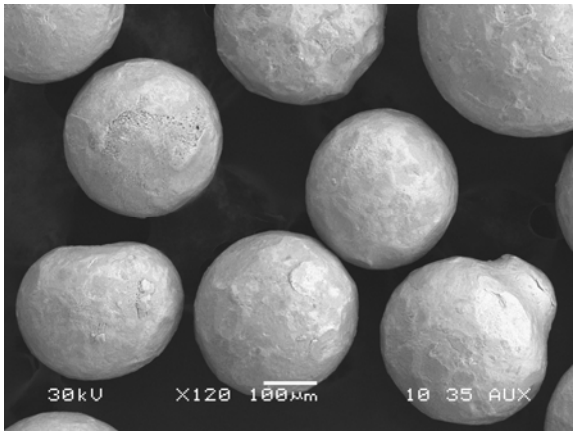

Figure 3-3. SEM Image of Unreacted Amasteel

3.2.2 Single-Pass Flow-Through (SPFT) Apparatus

Evaluation of each of the kinetic rate parameters is done with the SPFT test method. A general description of the SPFT system is provided in this section. For a more detailed discussion and advantages of the SPFT system, see McGrail et al. (2000).

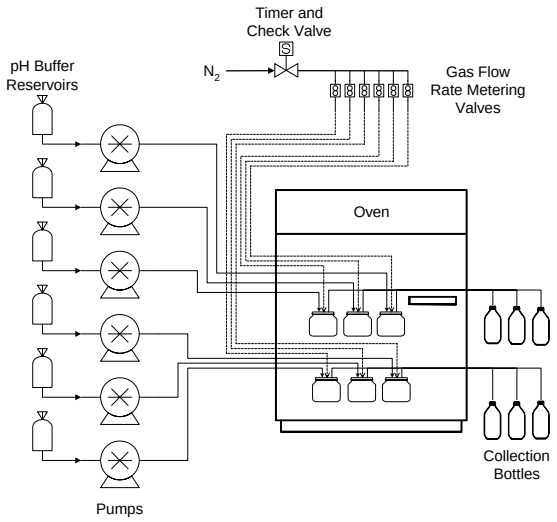

Figure 3-4. Schematic of the SPFT Apparatus

In general, the SPFT system (Figure 3-4) consists of a programmable pump that transfers solutions from an input reservoir through Teflon® lines to *perfluoroalkoxide* (PFA) Teflon reactors (Savillex, Minnetonka, MN). The reactor consists of two main pieces that thread together to form a cylinder that is 63-mm tall, with a 47.5-mm outer diameter, and a total inner volume of approximately 80 mL. The relatively large diameter of the reactor allows the metal particles to rest at the bottom; this creates a thin specimen layer and allows the metal particles to interact with the contacting solution. The reactors are placed in constant temperature ovens controlled to ±2°C with controllers connected to calibrated thermocouples. Solutions enter and exit through fluid transfer lines that pass through two separate ports in the top of each reactor. The residence time of aqueous solutions in the reactor varies with the flow rate, which is adjusted in accordance with the needs of the experiment. The fluid output line carries effluent solution to collection vials that are positioned outside the oven.

Effluent solution is collected continuously and aliquots of the fluid sample are retained for both pH measurement and chemical analyses with either inductively coupled-plasma mass spectroscopy (ICP-MS) or inductively coupled-plasma optical emission spectroscopy (ICP-OES). The ^{99}Tc concentrations were determined with the ICP-MS. Solutions earmarked for analysis with ICP-MS or ICP-OES methods are preserved with ultra-high purity nitric acid to a final concentration of 1% nitric acid. Concentrations of the dissolved components Fe, P, and ^{99}Tc quantify the dissolution rates as a function of pH and temperature. Solution samples from empty (blanks) SPFT reactors are collected and used to establish the concentration of background analytes, before the specimens are added to the reactors. The blank samples were collected once at the start of the experiment and were otherwise treated in exactly the same manner as the cells with the metal samples.

3.2.3 Buffer Solutions

The solutions used to control the pH during the SPFT experiments are summarized in Table 3-3, which also contains a summary of the pH values at each test temperature computed with the

Table 3-3. Composition of Solutions Used in SPFT Experiments. Solution pH Values Above 23°C Were Calculated With EQ3NR Code V7.2b Database.

Solution	Composition	pH @			
		23ºC	40ºC	70ºC	90ºC
1	0.05 M THAM + 0.047 M HNO_3	7.01	6.57	5.91	5.55
2	0.05 M THAM + 0.02 M HNO_3	8.32	7.90	7.25	6.89
3	0.05 M THAM + 0.0041 M HNO_3	8.99	8.67	8.08	7.72
4	0.05 M THAM + 0.003 M LiOH	9.99	9.55	8.88	8.52
5	0.0107 M LiOH + 0.010 M LiCl	11.00	10.89	10.43	10.06
6	0.0207 M LiOH + 0.010 M LiCl	12.02	11.74	11.08	10.70
THAM = *Tris* hydroxymethyl aminomethane buffer					

EQ3NR code (version 7.0; Wolery 1992). It is important to take into account the change in pH that occurs at different temperatures when computing dissolution rates from SPFT data because the in situ pH can vary by as much as 1.5 pH units over the temperature range of 23°–90°C. The pH values are always measured at room temperature (23°C) and the difference between the pH value measured and at temperature is not uniform for each solution over the pH range. For example, the difference between the pH(23°C) = 7.01 and pH(90°C) = 5.55 for solution 1 is not the same as for solution 3 where pH(23°C) = 8.99 and pH(90°C) = 7.72). These solutions were prepared by adding measured amounts of the organic *tris hydroxymethyl aminomethane* (THAM) buffer to deionized water (DIW) and adjusting the solution to the desired pH value with 15.8 M HNO_3 or 1 M LiOH. The THAM buffer range is between pH 7.0 and 10.0; therefore, the alkaline solutions in pH range 11.0 and 12.0 were prepared by adding LiOH and LiCl to DIW and adjusting the solution to the desired pH value with 15.8M HNO_3 or 1 M LiOH.

All experiments were conducted with solutions containing the metal complexant *ethylenediaminetetraacetic acid* (EDTA) by adding Na_2EDTA to the solutions described above. The EDTA minimizes the formation of the passive film (Sikora and Macdonald 2000), which eventually forms iron alteration phases, and helps keep the Fe ions in solution. This is an important consideration because of the low solubility of Fe(III) oxides and oxyhydroxides. Conducting these experiments with the SPFT system allows us to (1) maintain the pO_2 at a relatively constant level, (2) minimize the formation of a passivating layer, (3) prevent the precipitation of numerous Fe-bearing secondary phases, and (4) maintain dilute solution in contact with the iron specimen. Similar to SPFT tests with glasses, dilute solutions were achieved by adjusting the ratio of flow rate, q, to sample surface area, S.

3.2.4 Fe(III)-EDTA Complex Analysis

High pressure liquid chromatography (HPLC) was used to quantify the concentration of the Fe(III)-EDTA complex with a method developed by Nowack (2002). The mobile phase consisted of 92% 0.02 M formate buffer and 8% acetonitrile with 0.001 M tetrabutylammonium

bromide (TBA-Br). The formate buffer was made by mixing analytical grade sodium formate (~99% pure) with formic acid (89.5% pure). The HPLC system consists of an autosampler, HPLC pump and column, and a UV/VIS absorbance detector. The Gilson, Inc., (Middleton, WI) auto-sampler is fitted with a 500-µL syringe, 100-µL injection loop, and connected to a Gilson HPLC pump model 307. A Restek Corp. (Bellefonte, PA) Ultra C-18 HPLC column was used and is 205 mm in length, 4.6 mm in diameter, and 5 µm in packing diameter. Detection of the Fe(III)-EDTA complex was accomplished by setting the UV/VIS absorbance detector (Gilson Inc. model 119, Middleton, WI) to a wavelength of 258 nm. Calibration standards of Fe(III)-EDTA were prepared by adding equal molar amounts of $FeCl_3$ and Na_2EDTA; neither EDTA nor Fe^{3+} salts alone gave UV absorbance at 258 nm.

3.2.5 Dissolution Rate and Error Calculation

Dissolution rates, based on steady-state concentrations of elements in the effluent, are normalized to the amount of the element present in the sample by the following formula:

$$r_i = \frac{(C_i - \overline{C}_{i,b})q}{f_i S} \tag{2}$$

where

r_i = the normalized dissolution rate of the element i, in g/(m^2·d)

C_i = the concentration of the element, i, in the effluent (g/L)

$\overline{C}_{i,b}$ = the average background concentration of the element of interest (g/L)

q = the flow rate (L/d)

f_i = the mass fraction of the element in the Amasteel or ES-32B metal (dimensionless)

S = the surface area of the sample (m^2).

The value of f_i can be calculated from the chemical composition of the sample. Flow rates were determined from gravimetric analyses of the fluids collected in each effluent collection vessel upon sampling.

The average background concentrations were set by analyses of the starting input solution and three blank solutions. Typically, background concentrations of elements are below the sample-estimated limit of quantification (EQL). The sample EQL is determined by multiplying the sample dilution factor by the lowest calibration standard that can be determined reproducibly during an analytical run within 10%. In cases where the concentration of the analyte is at or below the EQL, the background concentration (blank value) of the element is set at the value of the EQL, even though the concentration of the element could be much lower. The EQL was 10 µg/L for Fe, 62.5 µg/L for P, and varied between 0.05 and 0.10 µg/L for ^{99}Tc as a function of how the ICP-MS was performing at the time of effluent analysis.

Determining the experimental uncertainty of the dissolution rate takes into account uncertainties of each parameter in Equation (2). For uncorrelated random errors, the standard deviation of a function $f(x_1, x_2,\ldots x_n)$ is given by:

$$\sigma_f = \sqrt{\sum_{i=1}^{n}\left(\frac{\partial f}{\partial x_i}\right)^2 \sigma_i^2} \tag{3}$$

where σ_f is the standard deviation of the function f., x_i is the parameter i, and σ_i is the standard deviation of parameter i. Substituting Equation (2) into Equation (3) results in:

$$\sigma_{r_i} = \sqrt{\left(\frac{q}{f_i S}\right)^2 \left(\sigma_{C_i}^2 + \sigma_{\overline{C}_{i,b}}^2\right) + \left(\frac{C_i - \overline{C}_{i,b}}{f_i S}\right)^2 \sigma_q^2 + \left(\frac{\left(C_i - \overline{C}_{i,b}\right)q}{f_i^2 S}\right)^2 \sigma_{f_i}^2 + \left(\frac{\left(C_i - \overline{C}_{i,b}\right)q}{f_i S^2}\right)^2 \sigma_S^2} \tag{4}$$

Equation (4) can also be expressed in terms of the relative error, $\hat{\sigma}_{r_i} = \sigma_{r_i} / r_i$, and is given by

$$\hat{\sigma}_{r_i} = \sqrt{\frac{\left(\hat{\sigma}_{C_i} C_i\right)^2 + \left(\hat{\sigma}_{\overline{C}_{i,b}} \overline{C}_{i,b}\right)^2}{\left(C_i - \overline{C}_{i,b}\right)^2} + \hat{\sigma}_q^2 + \hat{\sigma}_{f_i}^2 + \hat{\sigma}_S^2} \tag{5}$$

Relative errors of 10%, 10%, 5%, 3%, and 15% for C_i, $\overline{C}_{i,b}$, q, f_i, and S, respectively, are typical for measurements conducted at PNNL. Although the absolute error in f_i is likely higher than 3%, this error is non-systematic and therefore does not contribute significantly to sample-to-sample uncertainty, which is the principal error of interest here. The conservative appraisal of errors assigned to the parameters in Equation (5), in addition to the practice of imputing detection threshold values to background concentrations, results in typical uncertainties of approximately ±35% on the dissolution rate.

4.0 Modeling

The STORM code (Bacon et al. 2004) was used to simulate the weathering of BV waste packages after emplacement in the IDF. Input data to STORM can be divided into two parts: (1) unsaturated flow and transport and (2) chemistry. Entries for unsaturated flow and transport include lithographic units, hydraulic properties, and hydraulic initial and boundary conditions. These are described in Section 4.1. Chemistry input to STORM consists of entries for aqueous, gas, and solid species; equilibrium reactions; kinetic reactions; and geochemical initial and boundary conditions. These are described in Section 4.2. The output from STORM includes normalized Tc flux to the vadose zone and Tc concentrations in pore water surrounding the BV waste packages. These are described in Section 4.3.

4.1 Unsaturated Flow and Transport Input

4.1.1 Lithographic Units

To establish a consistent framework for overlaying a computational grid on the spatial domain of interest, a set of material zones or lithographic units are defined for units with similar hydrogeological and geochemical properties. These zones are usually related to disposal design components, geologic formations, or geologic lithofacies determined from borehole analyses. However, because there are practical limits to the resolution of the model grid, material zones may also include combinations of materials that are assigned uniform hydraulic and/or chemical properties. Classification of these materials into appropriate zones was performed as a part of the near-field hydraulics data package (Meyer et al. 2004).

Bulk vitrification waste packages containing 6-Tank Composite (BKV1) glass (Pierce et al. 2005) were simulated. Data on these waste materials and near- and far-field materials were principally defined from facility design documents (Puigh 2004), the near-field hydraulic properties data package (Meyer et al. 2004), or the far-field hydraulic properties data package (Khaleel 2004). The BV waste package simulation domain consists of four 2.44 x 2.44 m BV waste packages stacked in a column and separated by 0.86 m in the vertical direction. The waste packages are surrounded by backfill soil that overlies Hanford sand (Figure 4-1). Although the average waste package spacing was assumed to be 0.30 m, each waste package is offset 0.10 m horizontally relative to the package above and below. The total height of the trench is 17.8 m. The bottom of the lowest waste package is 4.6 m above the bottom of the modeled

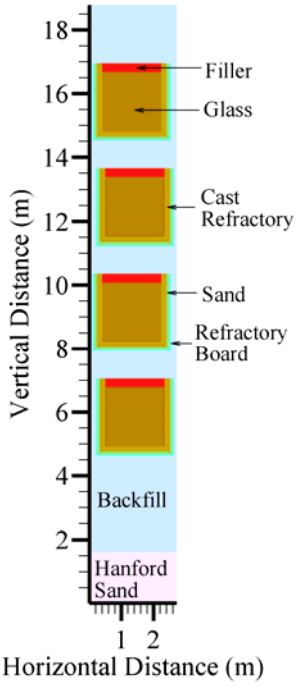

Figure 4-1. Lithographic Units for BV Waste Form Release Simulations

lithographic unit. The waste glass is surrounded by an insulating layer of cast refractory 0.16 m thick, a layer of insulating sand 0.08 m thick, and finally a layer of refractory board 0.06 m thick. Although the latter is in reality only located at the end of the BV box, it is modeled as surrounding the glass to provide uniformity to the modeled package and to simplify the calculation. The waste packages shown in Figure 4-1 are filled with glass to a height of 1.86 m. The rest of the package is filler material with the same hydraulic properties as backfill.

For each lithographic unit, a list of the solid species that make up the unit is required. For each solid, the relative volume and the specific surface area are needed. Initial values for these variables for each lithographic unit are listed in Table 4-1 and Table 4-2, respectively. For Hanford sands and backfill soil, petrologic and particle size data were obtained from the near-field hydrology data package (Meyer et al. 2004). The specific surface area was inferred from the particle size data. Assuming spherical grains, the average specific surface area A_m is related to the average particle radius R_m by

$$A_m = \frac{3V_r}{R_m\left(1-\theta_T\right)} \tag{6}$$

where V_r is the relative amount by volume of each mineral and θ_T is the total porosity. The relative amount of each mineral in each material should sum to a total value of one.

The assumed specific surface area for Hanford sediments and backfill soil are consistent with petrologic and particle size data obtained from laboratory-measured values (Serne et al. 1993). The specific surface area of the filler material in the WTP and BV waste packages is assumed to be the same as the backfill.

Table 4-1. Relative Amount by Volume of Solid Species in Material Zones

MATERIAL	Glass	Quartz	Albite	K-Feldspar	Illite	Mullite
Hanford Sand	0	0.4	0.4	0.1	0.1	0
Backfill	0	0.4	0.4	0.1	0.1	0
Refractory Board	0	0.4	0.4	0.1	0.1	0
Sand Insulation	0	1	0	0	0	0
Cast Refractory	0	0	0	0	0	1
Glass	1	0	0	0	0	0
Filler	0	0.4	0.4	0.1	0.1	0

The surface area assumed for the glass is consistent with the expected sparse degree of glass fracturing in the waste package based on prior experience with high-level waste glasses (Peters and Slate 1981; Farnsworth et al. 1985). Fracturing is expected to increase the glass surface area no more than 10 times its geometric surface area.

4.1.2 Computational Grid

The computational grid was set at 0.02 m in vertical resolution. This grid spacing was used to resolve the details in the BV waste packages and to resolve the backfill material between waste packages.

Table 4-2. Specific Surface Area (m^2/m^3) of Solid Species in Material Zones

MATERIAL	Glass	Quartz	Albite	K-Feldspar	Illite	Mullite
Hanford Sand	0	8200	8200	2050	41 000	0
Backfill	0	8200	8200	2050	41 000	0
Refractory Board	0	8200	8200	2050	41 000	0
Sand Insulation	0	20 000	0	0	0	0
Cast Refractory	0	0	0	0	0	25,000
Glass	50	0	0	0	0	0
Filler	0	8200	8200	2050	41 000	0

The calculation time step was determined automatically during the calculation with a convergence criterion of 1.5×10^{-7}. This ensures that predicted values of aqueous species concentrations and mineral volumes are accurate between iterations for a given time step. If this cannot be achieved within a certain number of iterations, the time step is automatically reduced. Numerous simulations were conducted to ensure that the grid spacing and convergence criteria selected for the simulations were small enough to obtain good accuracy, yet large enough to allow the simulations to finish in a reasonable amount of time. Results from these simulations were not significantly different from those with the grid spacing and convergence criterion used in the simulations reported in this document.

4.1.3 Material Hydraulic Properties

The hydraulic properties for each lithographic unit in the simulation were determined in the near-field hydraulics data package (Meyer et al. 2004) or the far-field hydraulic properties data package (Khaleel 2004). These properties are also reported in Table 4-3. The hydraulic properties for the BV glass were assumed to be the same as for WTP glass (Meyer et al. 2004). The glass is assumed to be fractured by an amount that would increase the surface area of the glass by a factor of 10 over unfractured glass. Because the thermal expansion coefficient for glass, 9.5×10^{-6} per degree C (Banal and Doremus 1986), is less than that for iron/steel, 12.1×10^{-6} per degree C (Perry and Green 1984), the metal inclusions are likely to shrink more upon cooling than the glass. Therefore, we do not assume that the metal inclusions would increase the amount of cooling fractures.

Based on particle size data, the hydraulic properties for the insulating sand were estimated from experimental measurements performed on similar sand (Mualem 1976). The filler and refractory board hydraulic properties were assumed identical to backfill. For the cast refractory,

unsaturated hydraulic properties for the matrix were taken from experimental data for clay brick ceramic (Hall and Hoff 2002). Hydraulic properties for the fractures in the cast refractory were assumed to be the same as the glass fractures.

Table 4-3. Material Hydraulic Properties Used in Simulations

Material	Particle Density (10^3 kg/m^3)	Saturated Water Content	Residual Water Content	van Genuchten α (m^{-1})	van Genuchten n	Saturated Hydraulic Conductivity (m/s)
Hanford Sand	2.63	0.394	4.9×10^{-2}	6.31	2.05	4.15×10^{-5}
Hanford Gravel	2.63	0.138	1.0×10^{-2}	2.10	1.37	6.60×10^{-6}
Backfill	2.71	0.350	3.00×10^{-2}	6.50	1.70	4.91×10^{-5}
Refractory Board	2.71	0.350	3.00×10^{-2}	6.50	1.70	4.91×10^{-5}
Sand Insulation	2.65	0.344	1.82×10^{-2}	3.70	3.90	7.64×10^{-5}
Cast Refractory (matrix)	3.10	0.170	6.29×10^{-4}	1.46	2.47	3.80×10^{-11}
Cast Refractory (fracture)	3.10	0.020	4.60×10^{-4}	20.0	3.00	1.00×10^{-4}
Glass	2.68	0.020	4.60×10^{-4}	20.0	3.00	1.00×10^{-4}
Filler	2.71	0.316	3.00×10^{-2}	6.50	1.70	4.91×10^{-5}

4.1.4 Hydraulic Boundary Conditions

The hydraulic conditions assumed for the BV waste form release calculations were steady-state flow under the following boundary conditions:

- The water flux was imposed at the upper boundary of the model at a rate of 0.1, 0.5, or 0.9 mm/y.
- The left and right boundaries are assumed to be the axes of symmetry, and are therefore the no-flux boundaries.
- The unit gradient is assumed at the lower boundary, where water flow is entirely due to the force of gravity, rather than a gradient in capillary pressure.
- Because the lower boundary is the only location where water can escape the model, the total water flux at the lower boundary is equal to the total water flux through the upper boundary, minus the water consumed in any chemical reactions between water and the glass and other materials in the IDF.
- The glass and sand drain easily, and so have low water contents (Figure 4-2).
- The backfill and filler material retain moisture more readily, and thus have higher water contents.

4.1.5 Solute Transport Coefficients

The aqueous diffusion coefficients were assumed to be 5 x 10^{-9} m^2/s for all aqueous species (Mann et al. 1998). The gas partial pressure for CO_2 and O_2 were fixed at atmospheric values of 0.03 kPa (3 x 10^{-4} atm) and 21 kPa (0.21 atm), respectively.

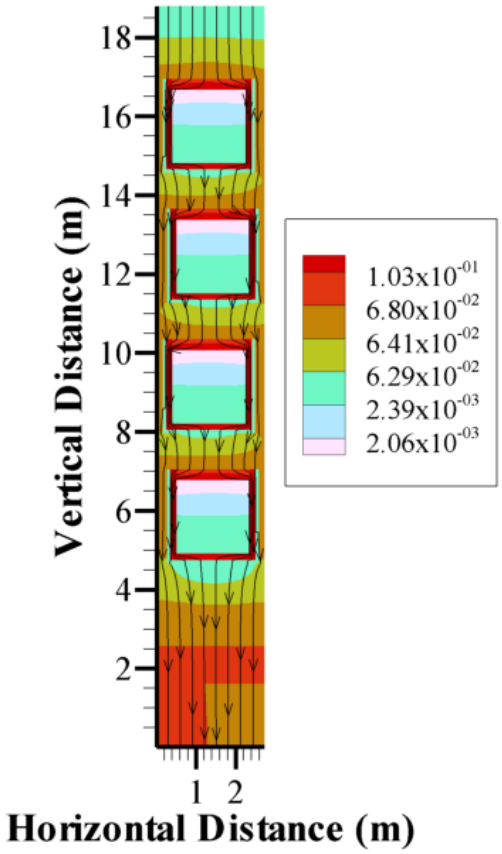

Figure 4-2. Water Content and Water Flow Stream Traces for BV Reactive Transport Simulations at 0.9 mm/y Recharge Rate

4.2 Chemistry Input

4.2.1 Aqueous Species

Aqueous species are the cations, anions, or neutral complexes present in the aqueous phase. The aqueous species listed in Table 4-4 were identified by simulating the dissolution of waste glass in deionized water at 15°C with the EQ3/6 code package (Wolery and Daveler 1992). All thermodynamic data were obtained from the EQ3/6 data0.com.R8 database (Daveler and Wolery 1992). The EQ3/6 software was used to extract a subset of aqueous species and mineral phases from the large thermodynamic database that were relevant for the reactive transport simulations.

Table 4-4. Key Aqueous Species Produced by the Dissolution of Waste Glass

Species	Species
AlO_2^-	KOH(aq)
$B(OH)_3(aq)$	Mg^{2+}
BO_2^-	$MgB(OH)_4^+$
Ca^{2+}	$MgCO_3(aq)$
CaB(OH)4+	$MgHCO_3^+$
CaCO3(aq)	Na^+
CaHCO3+	$NaB(OH)_4(aq)$
CaOH+	$NaCO_3^-$
$CO_2(aq)$	$NaHCO_3(aq)$
CO_3^{2-}	$NaHSiO_3(aq)$
$Fe(OH)_3(aq)$	NaOH(aq)
H_2O	$O_2(aq)$
$H_2SiO_4^{2-}$	OH^-
H^+	$SiO_2(aq)$
HCO_3^-	TcO_4^-
$HSiO_3^-$	$Ti(OH)_4(aq)$
K^+	$Zr(OH)_4(aq)$

4.2.2 Gases

Gas species are compounds such as CO_2 and O_2 that make up the air phase in STORM simulations. The partial pressures for each gas species are needed. Only CO_2 and O_2 are expected to influence the chemical environment significantly in the near and far fields.

4.2.3 Solid Phases

For each solid phase, including any secondary minerals that precipitate from supersaturated conditions, the mass density (kg/m^3) and the stoichiometric coefficient of each element are needed. The simulation results in the following sections reference the Six-Tank Composite waste glass formulation (Table 4-5).

The mass density of the Six-Tank Composite glass was determined to be 2.71×10^3 kg/m^3. The Tc composition of the glass was taken from the ES-32B test (AMEC 2005), where the average Tc concentration in five samples was 1.50 mg Tc/kg glass. Given that the molecular weight of the glass formulation given in Table 4-5 is 67.98 g/mol, the mol fraction of Tc in glass is then 1.03×10^{-6}.

The compositions of materials that make up the backfill, filler, Hanford soil, and cast refractory used in the simulations are listed in Table 4-6 (Serne et al. 1993).

Secondary phases are solids that precipitate from a supersaturated aqueous solution. A list of potential secondary phases that form from long-term weathering experiments with the various waste glass formulations and from modeling the solution chemistry observed in experiments with the EQ3/6 code is provided in Pierce et al. (2004b). Several phases were eliminated from

consideration because (1) formation of the phase is kinetically prohibited at the disposal system temperature of 15°C, (2) selection of the phase would violate the Gibbs phase rule, (3) simulations show that allowing the phase to form is inconsistent with a large body of laboratory test data with borosilicate glasses, or (4) the phase is unstable with respect to other minerals over the range of chemical environments expected for the IDF system.

Table 4-5. Chemical Formula of Six-Tank Composite (BKV1) Glass Used in Simulations

Element	Moles of Element / Moles of Glass
Al	1.22×10^{-1}
B	9.76×10^{-2}
Ba	2.22×10^{-4}
Ca	3.32×10^{-2}
Cl	3.45×10^{-3}
Cr	8.94×10^{-4}
F	2.50×10^{-3}
Fe	3.62×10^{-2}
K	2.22×10^{-2}
Mg	2.26×10^{-2}
Mn	6.70×10^{-4}
Na	4.38×10^{-1}
O	1.85
P	5.26×10^{-3}
S	7.13×10^{-3}
Si	5.23×10^{-1}
Tc	1.03×10^{-6}
Ti	6.72×10^{-3}
Zr	3.86×10^{-2}

Table 4-6. Composition of Native and Surrounding Materials Used in Simulations

Mineral	Formula	Molecular Weight, g/mol	Mass Density, 10^3 kg/m^3
Albite	$NaAlSi_3O_8$	262.2	2.6
Illite	$K_{0.6}Mg_{0.25}Al_{1.8}Al_{0.5}Si_{3.5}O_{10}(OH)_2$	383.9	2.75
K-Feldspar	$KAlSi_3O_8$	278.3	2.6
Quartz	SiO_2	60.1	2.7
Mullite	$3(Al_2O_3)2(SiO_2)$	426.1	2.6
Technetium Salt	KTcO4	201.1	2.6

The final phase assemblage used in the STORM simulations was further constrained because preliminary runs showed that a particular phase never formed or formed in such small amounts that the effects on the solution concentrations or other system properties were insignificant. The

composition of the secondary minerals used in the simulations is listed in Table 4-7. The mass density is obtained by dividing the molecular weight by the molar volume of the solid.

4.2.3.1 Metal Inclusions

The metal inclusions in the glass were assumed to consist mostly of iron, with 108 ppm of ^{99}Tc (AMEC 2005) (Table 4-8). Assuming that the metal inclusions consist mostly of iron with a molecular weight of 55.8 g/mol, the mole fraction of Tc in the metal inclusions is 6.1×10^{-5}. The mass ratio of metal to glass in the waste packages was assumed to be 0.48% (AMEC 2005).

Table 4-7. Composition of Secondary Minerals Used in Simulations

Mineral	Formula	Molecular Weight, g/mol	Mass Density, 10^3 kg/m^3
Anatase	TiO_2	79.8	3.9
Baddeleyite	ZrO_2	123.2	5.6
Calcite	$CaCO_3$	100.1	2.7
$Fe(OH)_3$(am)	$Fe(OH)_3$	106.9	3.1
Gibbsite	$Al(OH)_3$	78.0	2.4
Sepiolite	$Mg_4Si_6O_{15}(OH)_2{:}6H_2O$	647.8	2.3
SiO_2(am)	SiO_2	60.1	2.1

Table 4-8. Composition of Metal Inclusions Used in Simulations

Material	Formula	Molecular Weight	Mass Density, 10^3 kg/m^3
Metal	$FeTc_{0.000061}$	55.8	7.9

4.2.4 Equilibrium Reactions

For each equilibrium reaction, the stoichiometric coefficient of each aqueous species in each reaction and the equilibrium constant at a temperature of 15°C are needed. The equilibrium reactions in Table 4-9 were identified by simulating the dissolution of the waste glasses in deionized water at 15°C with the EQ3/6 code package (Wolery and Daveler 1992) and the data0.com.R8 database (Wolery and Daveler 1992; Daveler and Wolery 1992). Several secondary aqueous species were excluded from the simulations because their concentrations were extremely small over the range of chemical conditions anticipated for the IDF.

4.2.5 Kinetic Reactions

A full mass-action law type is used for each solid phase except the waste glass. A special mass-action law type implemented in the STORM code is used for the glass and is discussed in the following section.

Compilations of kinetic rate constants equivalent to thermodynamic databases for important mineral phases are not available. Also, the available mineral dissolution/precipitation kinetics data are limited much more than thermodynamic data. Consequently, sufficiently large rate constants are used to approximate equilibrium conditions, that is, to ensure that the phase will precipitate rapidly if the local chemical environment at a grid node is saturated with respect to the particular phase.

Table 4-9. Equilibrium Reactions at 15°C

Reaction	Log K
$BO_2^- + H_2O + H^+ = B(OH)_3(aq)$	9.35
$CO_2(aq) + H_2O = H^+ + HCO_3^-$	-6.42
$CO_3^{2-} + H^+ = HCO_3^-$	10.43
$CaB(OH)_4^+ = OH^- + B(OH)_3(aq) + Ca^{2+}$	-6.92
$CaCO_3(aq) + H_2O = OH^- + HCO_3^- + Ca^{2+}$	-7.15
$CaHCO_3^+ = HCO_3^- + Ca^{2+}$	-1.05
$CaOH^+ = OH^- + Ca^{2+}$	-1.49
$H_2SiO_4^{2-} + H^+ = 2\ H_2O + SiO_2\ (aq)$	22.96
$HSiO_3^- + H^+ = SiO_2(aq) + H_2O$	10.10
$KOH(aq) + H^+ = H_2O + K^+$	14.46
$MgB(OH)_4^+ + H^+ = H_2O + B(OH)_3(aq) + Mg^{2+}$	7.35
$MgCO_3(aq) + H^+ = HCO_3^- + Mg^{2+}$	7.50
$MgHCO_3^+ = HCO_3^- + Mg^{2+}$	-1.04
$NaB(OH)_4(aq) + H^+ = B(OH)_3(aq) + Na^+ + H_2O$	8.97
$NaCO_3^- + H^+ = HCO_3^- + Na^+$	9.82
$NaHCO_3(aq) = HCO_3^- + Na^+$	-0.24
$NaHSiO_3(aq) + H^+ = Na^+ + SiO_2(aq) + H_2O$	8.36
$NaOH(aq) + H^+ = Na^+ + H_2O$	15.12
$OH^- + H^+ = H_2O$	14.34

4.2.5.1 Glass Rate Law

For a dissolution reaction involving glass, parameters associated with the following kinetic rate law are needed:

$$r_g = \vec{k} a_{H^+}^{-\eta} e^{\frac{-E_a}{RT}} \left[1 - \left(\frac{Q}{K_g} \right)^{\sigma} \right] \tag{7}$$

where

r_g = dissolution rate, g/(m^2·d)
$\vec{k}$ = intrinsic rate constant, g/(m^2·d)
a_{H^+} = hydrogen ion activity (variable to be calculated by STORM)
E_a = activation energy, kJ/mol

R = gas constant, kJ/(mol·K)
T = temperature, K (assumed constant at 15°C)
Q = ion activity product for glass (variable to be calculated by STORM)
K_g = pseudo-equilibrium constant
η = pH power law coefficient
σ = Temkin coefficient ($\sigma = 1$ assumed).

Equation (7) is an approximation for glass because glass is thermodynamically unstable with respect to alteration products. Thus, equilibrium between glass and an aqueous solution containing all the glass components cannot occur. Equation (7) is an accurate description of the glass dissolution kinetics because the aqueous species involved in the rate-limiting step of the dissolution mechanism contains only silica. Many studies over the past 20 years have shown this species to be H_4SiO_4. The kinetic parameters in Equation (7) ($\vec{k}$, E_a, K_g, and η) have been determined for BV glasses by Pierce et al. (2004b); these values are given in Table 4-10.

Test results with BV glasses show that they are susceptible to a second reaction mechanism, alkali ion exchange. This reaction results in the selective extraction of Na,

$$\text{BKV1-Na} + H^+ \rightarrow \text{BKV1-H} + Na^+ \qquad (8)$$

where BKV1-Na represents the unreacted glass containing Na and BKV1-H represents a hydrated glass where the Na has been replaced with an equimolar amount of hydrogen. The rate of this reaction has been determined from SPFT experiments (Pierce et al. 2004b). In the STORM code, the amount of hydrated glass formed according to Equation (8) is tracked and then allows the glass to dissolve according to the same kinetic rate law Equation (7) as the parent glass.

Table 4-10. Summary of Kinetic Rate Parameters Used for Glasses

Parameter	Meaning	BV Six-Tank
$\vec{k}$	Intrinsic rate constant, mol/(m^2·s)	1.7×10^{-1}
K_g	Apparent equilibrium constant for glass based on activity of SiO_2(aq)	$10^{-2.85}$
η	pH power law coefficient	0.5
E_a	Activation energy of glass dissolution reaction, kJ/mol	75
r_x	Na ion-exchange rate, mol/(m^2·s)	4.0×10^{-11}

4.2.5.2 Bulk Vitrification Surrounding Materials

The BV waste glass is enveloped by cast refractory. Based on XRD analysis, the cast refractory was assumed to consist of mullite, $3(Al_2O_3)2(SiO_2)$ (Pierce et al. 2004b). Kinetic parameters for

mullite were determined from product consistency tests (Pierce et al. 2004b) and are given in Table 4-11, while the equilibrium constant was estimated from published thermodynamic data (Robie et al. 1978).

Table 4-11. Kinetic and Equilibrium Geochemical Parameters for Mullite

Symbol	Parameter	Value
k	Intrinsic rate constant, mol/(m^2·s)	1.22 x 10^{-4}
η	pH power law coefficient	0.34
E_a	Activation energy, kJ mol^{-1}	60.2
K_g	Log equilibrium constant	0.966

Based on experimental observations, soluble Tc is assumed to be evenly distributed in a 0.02-m zone in the cast refractory next to the sides of the glass. The initial amount of Tc in the cast refractory is assumed to be 0.3% of the total amount in the waste package (McGrail et al. 2003).

4.2.5.3 Secondary Phases

Pierce et al. (2004a,b) describe the methods used to develop a solubility product for the key secondary phases identified from laboratory testing and from simulations with the EQ3/6 code. The log K they derived for each secondary phase is given in Table 4-12.

Table 4-12. Secondary Phase Reaction Network and Equilibrium Constant (log K)

Reaction	log K (15°C)
Anatase + $2H_2O \rightleftharpoons Ti(OH)_4(aq)$	-6.56
Baddeleyite + $2H_2O \rightleftharpoons Zr(OH)_4(aq)$	-6.79
Calcite + $H^+ \rightleftharpoons Ca^{2+} + HCO_3^-$	2.00
$Fe(OH)_3(am) + H_2O \rightleftharpoons Fe(OH)_3(aq)$	-11.09
Gibbsite $\rightleftharpoons AlO_2^- + H_2O$	-13.10
Sepiolite + $8H^+ \rightleftharpoons 4Mg^{2+} + 6SiO_2(aq) + 11H_2O$	31.29
$SiO_2(am) \rightleftharpoons SiO_2(aq)$	-2.85

4.2.5.4 Soluble Technetium Salt

The release of the soluble Tc-bearing salt is limited by the diffusion coefficient assumed for the diffusion of the salt in the water within the pores of the cast refractory. An empirical model was used to calculate the diffusion coefficient for Tc, based on experimental data for the backfill and Hanford sand (Meyer and Serne 1999)

$$D_i = 1.486 D_f \theta^{1.956} \tag{9}$$

where D_f is the free water diffusion coefficient and θ is the water content. The dispersivity was assumed to be 10 mm based on the 20 mm grid size of the model to restrict the Peclet number (Bear 1979) to a maximum value of 2.

4.2.5.5 Metal Inclusions

The corrosion rate for metal inclusions in the glass was assumed to be equal to the low end of the field rates described in Section 3.1, 1.6×10^{-13} m/s (0.2 mil/year). Given the molecular weight and mass density assumed for the metal inclusions in Table 4-8, the metal inclusions were therefore assumed to have a corrosion rate of 2.3×10^{-8} mol/(m^2·s). The metal inclusion corrosion rate is two orders of magnitude greater than the glass corrosion rate at a recharge rate of 0.9 mm/y (Bacon and McGrail 2005).

Because the metal inclusions consist mostly of iron, the corrosion reaction and equilibrium coefficient for the metal inclusions (Table 4-13) were assumed to be the same as those of metallic iron (Wolery and Jarek 2003). The Tc in the metal inclusions is assumed to be released congruently as soluble TcO_4^-.

Table 4-13. Metal Inclusion Corrosion Reaction and Equilibrium Constant (log K)

Reaction	log K (15°C)
$Metal + 0.75O_2(aq) \rightleftharpoons Fe(OH)_3(aq) + 0.000061TcO_4^-$	54.15

Metal inclusions sealed inside waste glass are likely protected from corrosion until the waste glass itself corrodes. At a recharge rate of 0.9 mm/y, only 3.8% of the glass has corroded after 4300 years (Bacon and McGrail 2005). Therefore, the corrosion rate of metal inclusions was assumed to be limited by the exposure of the metal inclusions by fractures initially in the glass. Only inclusions exposed to the water flow in glass fractures were allowed to corrode at the maximum rate of 2.3×10^{-8} mol/(m^2·s), the remainder corroded at the glass rate, which is two orders of magnitude lower at a recharge rate of 0.9 mm/y (Bacon and McGrail 2005). Metal inclusions were assumed to have a uniform initial diameter, *d*, for each simulation. Only the inclusions that would fall within a distance *d* of the glass fractures were allowed to corrode at the maximum rate (Figure 4-3).

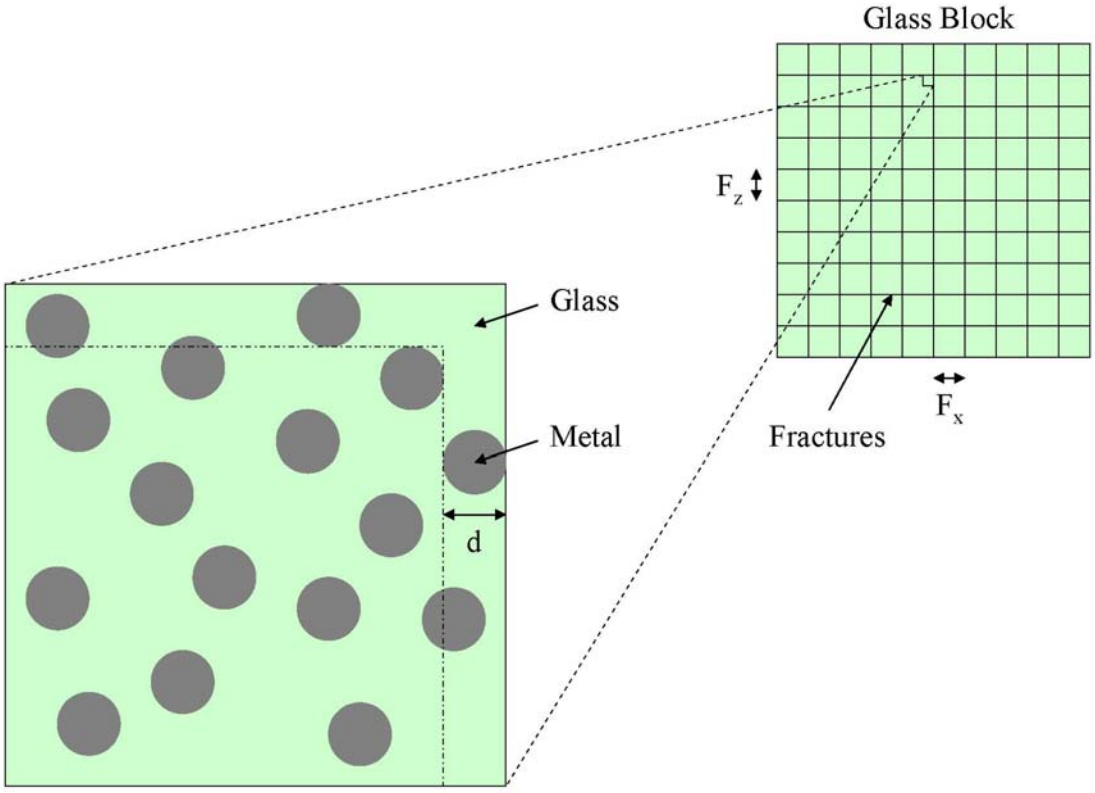

Figure 4-3. Metal Inclusions in Waste Glass with Regularly Spaced Fractures

In three dimensions, it is assumed that the fraction of metal inclusions exposed by fractures is equal to the proportion of glass by volume, which is within one metal inclusion diameter of a fracture, and is given by

$$V_{\text{exposed}} = \frac{2d\left(F_x F_y + F_x\left(F_z - 2d\right) + \left(F_y - 2d\right)\left(F_z - 2d\right)\right)}{F_x F_y F_z} \tag{10}$$

where F_x = fracture spacing in the x-direction, F_y = fracture spacing in the y-direction, F_z = fracture spacing in the z-direction, d = metal inclusion diameter.

This equation is based on the assumption that glass fractures will increase the glass surface area by a factor of 10 over an unfractured glass block, and the simplifying assumption that there will be an equal number of fractures in each direction. This means that there will be nine fractures in each direction. Given a rectangular glass block 1.84 x 1.86 x 6.9 m in size, F_x = 0.204 m, F_y = 0.207 m, and F_z = 0.767 m. Table 4-14 gives the percentage of metal inclusions exposed by glass fractures for various inclusion diameters.

Table 4-14. Percentage of Metal Inclusions Exposed by Glass Fractures

Metal Inclusion Diameter, mm	Exposed Inclusions, %
0.1	0.2
0.2	0.4
0.5	1.1
1	2.2
2	4.4
4	8.6
8	16.7

4.2.6 Initial and Boundary Conditions

For each specified gas species concentration, the partial pressure of gaseous species is needed. The gas partial pressures for CO_2 and O_2 were fixed at atmospheric values of 0.03 kPa (3×10^{-4} atm) and 21 kPa (2.1×10^{-1} atm), respectively.

For each specified aqueous species, the specified total concentration and the stoichiometric coefficient are needed. Aqueous species concentrations at the upper boundary and for initial conditions were specified as a part of the IDF geochemistry data package (Krupka et al. 2004) and are given in Table 4-15. Aqueous species concentrations were specified at the upper boundary, and a no diffusion condition was imposed across the lower boundary. The contaminant flux across the lower boundary was therefore limited to advection:

$$f = c\rho_w v \tag{11}$$

where

c = concentration (mol/kg)
ρ_w = density of water (kg/m^3)
v = specific discharge (m/s).

4.3 Model Output

The normalized flux of Tc to the vadose zone is calculated by summing the flux at each node across the bottom boundary of the model and normalizing the total flux according to the amount of each radionuclide in all the waste packages at the start of the simulation. The normalized flux across the lower boundary, F, in units of My^{-1} (My = million years), was calculated from

Table 4-15. Initial Aqueous Concentrations Used in Simulations

Species	Initial Concentration (mol/kg)
AlO_2^-	10^{-6}
$B(OH)_3(aq)$	10^{-10}
Ca (total)	10^{-7}
$Fe(OH)_3(aq)$	10^{-10}
H_2O	1
H^+	10^{-7}
K^+	10^{-6}
La^{3+}	10^{-10}
Mg^{2+}	10^{-10}
Na^+	10^{-6}
Si (total)	10^{-5}
TcO_4^-	10^{-10}
$Ti(OH)_4(aq)$	10^{-10}
$Zr(OH)_4(aq)$	10^{-10}

$$F = \frac{\sum_{i=1}^{N} f_i \Delta x_i \Delta y_i}{I_{Tc}} \zeta \tag{12}$$

where

f_i = flux across the bottom of an individual grid block (mol/(m^2·s))

$\Delta x_i \Delta y_i$ = cross-sectional area of an individual grid block (m^2)

ζ = the time conversion factor, where

$$\zeta = \frac{3.1558 \times 10^{13}\,\text{s}}{\text{My}} \tag{13}$$

I_{Tc} = inventory of Tc in the simulated waste packages (mol), where

$$I_{Tc} = V_{wp}\left(1-\theta_T\right)\rho_G \gamma_{Tc} \tag{14}$$

where

V_{wp} = volume of the waste packages (m^3)

θ_T = total porosity of the material representing the waste packages (m^3/ m^3)

ρ_G = molar density of the material representing the waste packages (mol/m^3)

γ_{Tc} = mole fraction of Tc in the material representing the waste packages (mol/mol)

The volume of the four simulated waste packages, V_{wp}, was 13.7 m^3 for the BV glass simulations. The cross-sectional area of each grid block was 0.02 m^2.

The units of My^{-1} are equivalent to units of "ppm/y," which were used in previous PAs (Mann et al. 2001; Mann et al. 1998). The term "ppm" was used to express the fraction of radionuclide

released from the waste packages per year in "per millionth," similar to the commonly used percent term. However, the unit ppm, when used in environmental science for expressing levels of pollutants in water, has the specific meaning of mg/liter (mg of contaminant per liter of water). Using ppm to mean "per millionth," while correct, may be confusing in this context and has been replaced with units of My^{-1}.

The Tc concentrations are also normalized to the inventory,

$$\mathrm{Tc}_{normalized} = \frac{\mathrm{Tc}}{I_{\mathrm{Tc}}} \tag{15}$$

5.0 Results and Discussion

5.1 Experimental Results

5.1.1 Amasteel SPFT Test Results

Although extensive information is available on the synthesis of α-Fe, there is no published information available on the formation of a ^{99}Tc-bearing Fe metal. Therefore, in some of the early scoping tests, commercially available α-Fe (Amasteel, a low carbon steel from Ervin Technologies) was used as a surrogate for the ^{99}Tc-bearing Fe metal phase found in the glass product from the ES-32B test. The purpose of the scoping tests was to determine test conditions under which the dissolution rate of the iron was independent of flow rate (q/S, see below) and EDTA concentration (see below). In addition, the partial pressure of O_2 in the air above the solution in the SPFT reservoir needed to be increased so that the dissolved concentration of O_2 was the same at 90°C as at room temperature. These results were also used to evaluate the difference between the low carbon steel and ES-32B metal sample.

5.1.1.1 Effect of Flow Rate, *q*, to Sample Surface Area, *S*, on Elemental Release Rates

Figure 5-1 illustrates the effect of varying the ratio of flow rate, q, to sample surface area, S. The q/S is manipulated either by changing the flow rate or changing the mass of sample or average particle size used in a test. Rates based on concentrations of iron are plotted for the conditions of 90°C, pH (23°C) = 9.0. This figure illustrates that as q/S increases, dissolution rates increase to a constant value [35.5 ±10.1 g/(m^2·d) or 66.3 ±18.9 mil/y at $\log_{10}$ (q/S), [m/s] ≈ -4.8]. The selection of $\log_{10}$ (q/S), [m/s] ≈ -4.8 as the appropriate q/S is somewhat arbitrary in this case; normally the break point in the data is more definitive. Clearly by $\log_{10}$ (q/S), [m/s] ≈ -6, the dissolution rate decreases with further decreases in q/S. At high q/S, the iron dissolution rate is independent of solution saturation state; that is, further increases in the q/S no longer produce an increase in the dissolution rate. Under these conditions, the dissolution rate is at the maximum or forward rate of reaction (Åagaard and Helgeson 1982). This allows the effect of potential rate-influencing variables, such as pH, temperature, and solution composition, to be independently varied allowing the rate-law (Equation (7) to be parameterized.

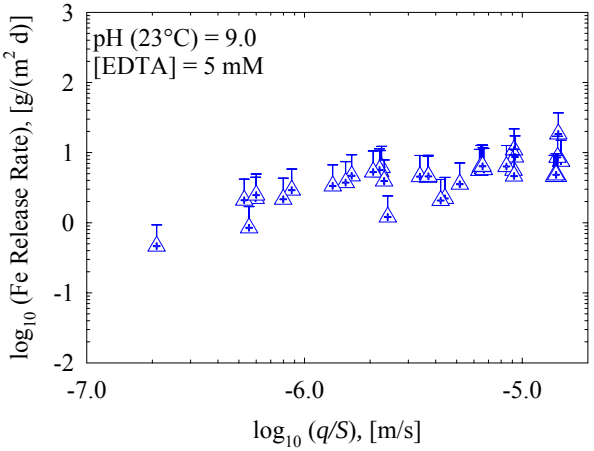

Figure 5-1. Iron ($\log_{10}$) Release Rate as a Function of $\log_{10}$ q/S (ratio of flow rate to surface area) at 90°C, pH(23°C) = 9.0.

For example, the hydrogen ion effect can be determined by conducting experiments as a function of pH while maintaining a constant aqueous O_2 concentration.

5.1.1.2 Dependence of Dissolution Rate on EDTA Concentration

All experiments were conducted with solutions containing EDTA. As with *q/S*, it is important to adjust the EDTA concentration until further increases no longer change the measured dissolution rate. This is because the addition of EDTA minimizes the formation of iron alteration phases and helps maintain a low uncomplexed Fe concentration by forming an aqueous Fe-EDTA complex. Dissolution kinetics of Amasteel was quantified as a function of EDTA concentration, from 0.01 to 5 mM, at pH(23°C) = 9.0 and T = 90°C.

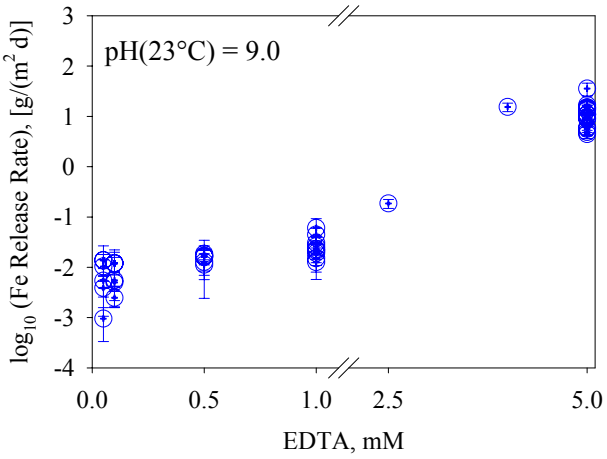

Figure 5-2. Iron ($\log_{10}$) Release Rate as a Function EDTA Concentration at Various $\log_{10}$ *q/S* (ratio of flow-rate to surface area), T = 90°C, and pH(23°C) = 9.0.

Figure 5-2 illustrates the effect of varying the concentration of EDTA on the release of iron from the dissolution of Amasteel. Under dilute conditions, EDTA concentrations less than approximately 1.0 mM, the release of iron from Amasteel is weakly dependent on the EDTA concentration because the concentration of Fe is controlled by the precipitation and dissolution of iron hydroxides and oxyhydroxides. Increasing the EDTA concentration above 1.0 mM causes an increase in the dissolution rate until it is approximately constant at an EDTA concentration of 4 to 5 mM where the dissolution rate of Amasteel is 35.5 ±10.1 g/(m^2·d) (66.3 ±18.9 mil/y) at $\log_{10}$ (*q/S*), [m/s] ≈ -4.8.

We attempted to determine the concentration of EDTA in solution with ion chromatography, but the analysis was unsuccessful due to detection limit problems. This attempt was made to verify the concentration of EDTA in the starting and ending solution.

Absorption of EDTA facilitates dissociation of the oxidized surface complex while minimizing the formation of a partially oxidized surface-layer and/or solubility-limiting Fe phase(s) by forming an aqueous Fe(II)-EDTA complex (Wehrli et al. 1989). Subsequently, the aqueous Fe(II)-EDTA complex is rapidly transformed to the Fe(III)-EDTA complex (Santana-Casiano et al. 2000), which exhibits a limited absorptivity allowing the Fe-EDTA complex to be transported away from the surface (Nowack and Sigg 1996; Wehrli et al. 1989). As such, the dissolution of Amasteel is surface-controlled (not transport-controlled) and is proportional to the surface concentration of the complex that enhances dissolution (Bondietti et al. 1993). The maximum dissolution rate as a function of EDTA concentration occurs at the maximum surface

Fe-EDTA complex concentration. This agrees with previous investigations that demonstrated the rate of dissolution reaches an apparent maximum at high adsorbed EDTA concentrations (Rubio and Matijevic 1979; Chang and Matijevic 1983; Ballesteros et al. 1998).

Aqueous Fe(II) readily reacts with oxygen, and may alter the apparent dissolution rate due to changes in redox conditions within the system and/or the formation of secondary precipitates. Several other changes in the aqueous speciation are occurring over the same pH range. Above a pH(23°C) value of about 6.5, EDTA is less effective at complexing Fe(III), decreasing by 3 orders of magnitude for each unit pH increase. There are a number of $Fe(OH)_x^{(3-x)}$ complexes where x varies from 1 to 4 (Lindsay 1979). The cationic species decrease in concentration with increasing pH, while the anionic complex (x = 4) increases in concentration with increasing pH – one order of magnitude for each unit pH increase. Between pH(23°C) = 7.5 and 8.5, the neutral species (invariant with pH) is the dominant species while the anionic species (x = 4) becomes increasingly dominant above a pH(23°C) value of 9.0. This complex chemistry complicates the interpretation of the dissolution rate data in the pH(23°C) range 10.0 to 12.0 as elaborated in the following paragraph. Further experimentation would be required to determine the effect of this complex Fe(III) chemistry on the dissolution rate.

As a quadraphonic acid, EDTA is progressively deprotonated with increasing pH. At pH(23°C) values greater than 10.24, EDTA is fully deprotonated, which effectively keeps EDTA from adsorbing onto the Fe surface (Blesa et al. 1984). Over the pH(23°C) range of 6.12 to <10.24, the dominant EDTA species in solution is a mono-protonated ligand that is capable of binding to the Fe surface to form the Fe-EDTA complex, which promotes dissolution. However, the addition of OH^- into the iron coordination sphere occupies positions that, under more acidic conditions, are available to coordinate with EDTA functional groups. As the solution pH becomes more alkaline and the concentration of hydroxide ions increases, competition between OH^- and EDTA increases for Fe complexation until Fe-hydroxide complexes become dominant. This decrease in the Fe-EDTA complexes imparts additional negative charge, weakening the remaining Fe-EDTA chelate bonds and increasing the dissociation kinetics as a function of pH (Sunda and Huntsmann 2003; Gambardella et al. 2005). At pH(23°C) ≥ 10.24, adsorption of EDTA onto Amasteel is inhibited resulting in surface complexation by hydroxyl ions or the release of iron hydroxide complexes into solution, which may undergo secondary precipitation as iron oxyhydroxides (Rubio and Matijevic 1979).

Chang and Matijevic, (1983) proposed a dissolution mechanism for hematite in the presence of EDTA where, in acids, dissolution proceeds through adsorption of EDTA to the surface followed by removal of Fe-EDTA complexes, and in alkaline solutions, Fe ions released into solution react with either aqueous hydroxide or chelating ions. This mechanism was supported by results of further studies on a variety of iron hydroxide minerals that indicate, in the presence of EDTA, the oxidation of iron is not affected by a change in pH(23°C) from 6.0 to 8.2. Instead, the speciation of Fe(II) is controlled by the concentration of EDTA (Santana-Casiano et al. 2000). Adsorption of EDTA onto goethite (Stumm 1997; Rubio and Matijevic 1979; Nowack and Sigg

1996; Nowack and Sigg 1997; Rueda et al. 1985), lepidocrocite (Bondietti et al. 1993; Rubio and Matijevic 1979), magnetite (Blesa et al. 1984), hematite (Chang and Matijevic 1983) and hydrous ferric oxide (Nowack and Sigg 1997) decreases as solution alkalinity increases, becoming negligible at pH(23°C) ≥ 10.

A select set of dissolution tests was run in the presence of air enriched with O_2 to compensate for the decrease in gas solubility with increasing temperature. At 23°C, the concentration of O_2 in water [O_2 (aq)] in equilibrium with air (21 vol% O_2) is 8.8 ppm. To compensate for the reduced gas solubility at 90°C, air with 32 vol% O_2 was used so that equilibrium dissolved O_2 was also 8.8 ppm. Figure 5-3 illustrates the calculated dissolution rate of Amasteel in solutions with pH(23°C) = 9.0, 11.0, and 12.0 (Table 3-3), and T = 90°C, is independent of additional oxygen. (The reader should note that the pH values plotted in Figure 5-3 and others are those calculated from the pH(23°C) values; see Table 3-3)

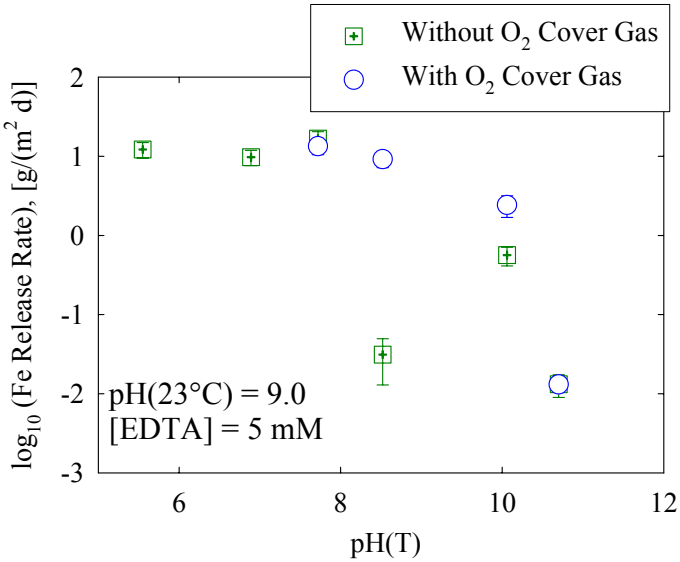

Figure 5-3. Iron ($\log_{10}$) Release Rate at 90°C as a Function of pH(23°C), from 7.0 to 12.0, at 2.9 ppm and 8.8 ppm Oxygen

However, at pH(23°C) = 10.0, 90°C, the dissolution rate displays an apparent oxygen dependency. The results of SEM analyses of post-reacted materials at pH(23°C) ≤ 10.0, in the presence and absence of added oxygen, do not indicate the formation of secondary phases (Figure 5-4). However, Amasteel sample that had been in a SPFT test at pH(23°C) > 10.0 showed evidence of a secondary iron oxide phase when examined in the SEM-EDS. The analysis of the secondary phases suggested a composition of 51.39 mass% Fe, 43.43 mass% O, and trace quantities of Na

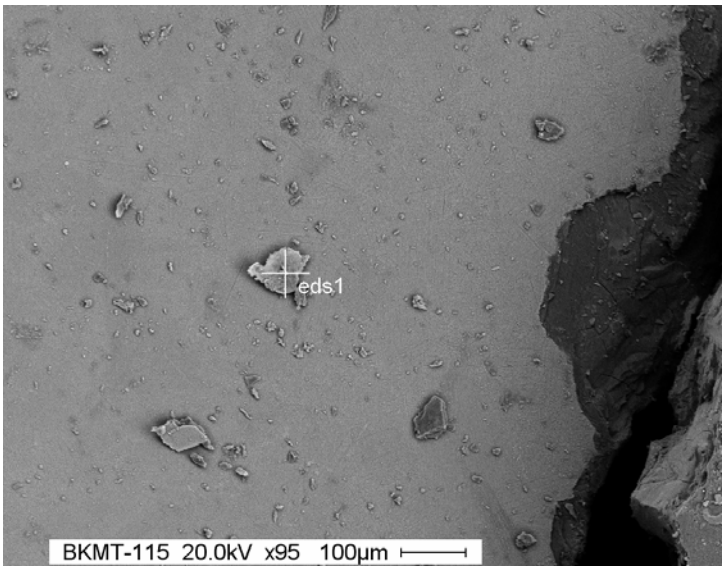

Figure 5-4. Scanning-electron Micrograph of Post-reacted Zero Valent Iron, 90°C, pH (23°C) = 10.0 (image is representative of post-reacted zero valent iron 90°C, pH (23°C) = 7.0 - 10.0). There is no Observable Formation of Secondary Phases.

and Cl (Figure 5-5) in the presence and absence of added oxygen. This result further suggests the reason for the observed changes is from a variation in the solution species with increasing pH (see the above discussion on the changes is solution species).

Analyses with HPLC of samples collected over the pH(23°C) range of 10.0 to 12.0 in the presence and absence of additional oxygen indicate that in the presence of additional oxygen, the concentration of Fe(III)-EDTA complexes in solution is two orders of magnitude greater at pH(23°C) = 10.0 and approximately an order of magnitude greater at pH(23°C) = 11.0 than in the solutions where no additional oxygen was present. The aqueous Fe(III)-EDTA complex was not detected at pH(23°C) = 12.0 (Table 5-1). This suggests that complexation of aqueous iron by EDTA and hydroxyl ions at pH(23°C) = 10.0 results in further release of iron from the solid increasing the apparent dissolution rate (Chang and Matijevic 1983). However, for solution with pH(23°C) values between 11.0 and 12.0, the apparent dissolution rate of Amasteel is inversely dependent on the concentration of hydroxide and is influenced by the formation of secondary iron oxyhydroxide phases (Bondietti et al. 1993; Rubio and Matijevic 1979).

Table 5-1. Concentration of Fe(III)-$EDTA_{(aq)}$ (M) in the Presence and Absence of Oxygen Cover Gas

pH(23°C)	Ambient	Oxygen
10	6.4×10^{-6}	4.7×10^{-4}
11	1.1×10^{-5}	3.4×10^{-4}
12	ND	ND
ND = Not Detected		

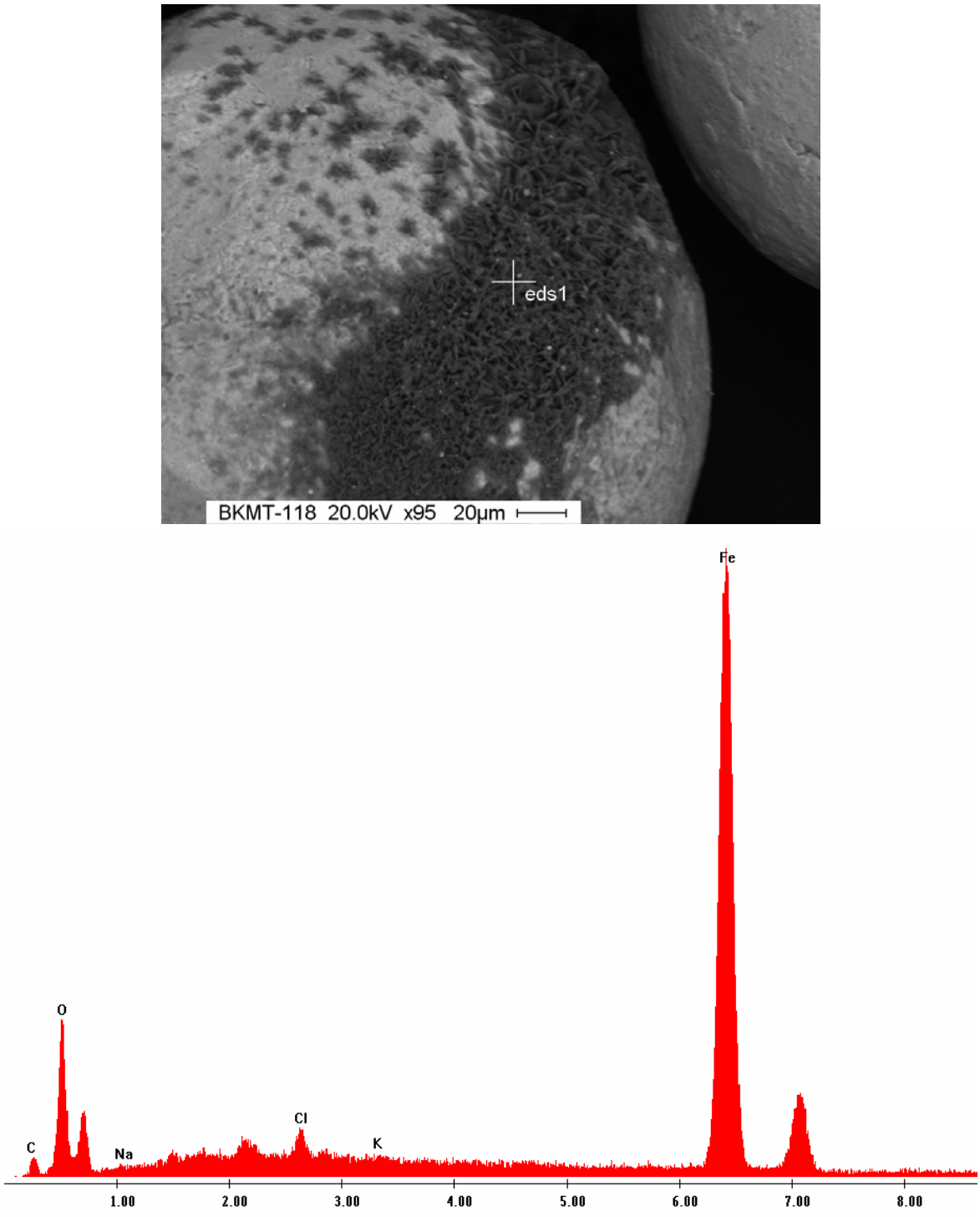

Figure 5-5. Scanning-electron Micrograph of Post-reacted Zero Valent Iron, 90, pH(23°C) = 12.0 (image is representative of post-reacted zero valent iron 90°C, pH(23°C) = 11.0 to 12.0) (top). Energy Dispersive Spectroscopy Analysis of Secondary Phase Noted in SEM Image (bottom). EDS Spectra Suggest the Formation of a Secondary Iron Oxide Phase.

5.1.2 ES-32B SPFT Test Results

After determining the appropriate *q/S* in the presence of 5 mM EDTA, additional experiments with the EST-32B phase were conducted as a function of pH(23°C), from 7.0 to 12.0, and temperature from 23 to 90°C. These experiments were performed to evaluate the effect of pH and temperature on the Fe metal dissolution rate, thereby allowing us to develop rate-law parameters; evaluate the effect, if any, on what the presence of P and ^{99}Tc in the ES-32B metal phase may have on the overall corrosion rate; and to compare the results obtained from the ES-32B metal phase to the results obtained with Amasteel.

As previously stated, experiments were conducted over a set of pH(23°C) values, from 7.0 to 12.0, and temperature, from 23°C to 90°C, to evaluate the effect of pH and temperature on the rate of metal dissolution. The *in situ* solution pH has been corrected for the effect of temperature with the EQ3NR code [version 7.0 (Wolery 1992), see Table 3-3]. Figure 5-6a, b, and c show that steady-state dissolution rates based on Fe, P, and ^{99}Tc, respectively, were reached at each temperature (23°, 40°, 70°, and 90°C) as a function of pH(*T*), from 7.0 to 12.0. The measured pH is always at room temperature, pH(23°C). The results from the calculations show that, as pH increases from 7.0 to 10.0, the overall dissolution rate decreases by a small amount. For example, the dissolution rate, based on ^{99}Tc, at T = 90°C was approximately 7 times lower at pH(23°C) = 7.0 (r_{Tc} = 7.0 ±1.5 g/(m^2·d) or 14.9 ±3.3 mil/y), compared to pH(23°C) = 10.0 (r_{Tc} = 1.0 ±0.2 g/(m^2·d) or 2.1 ±0.5 mil/y). A similar decrease in the dissolution rate was observed for Amasteel. The observed decrease in the dissolution rate may be the result of changes in the EDTA and iron speciation. Additional data are needed. As previously stated in Section 5.1.1.2, EDTA deprotonates at pH (23°C) > 10.0, which decreases the formation of the Fe-EDTA complex and causes a decrease in the observed dissolution rate.

Similar to pH, ES-32B metal dissolution was also found to be relatively insensitive to temperature. This can also be seen in Figure 5-6a, b, and c, where the dissolution rate, based on Fe, P, and ^{99}Tc, illustrates a small increase with increasing temperature. These results show as much as a three-fold increase in dissolution rate with a 67°C temperature increase. For example, at pH(23°C) = 9.0 the average steady-state ^{99}Tc release rate increases from r_{Tc} = 0.9 ±0.2 g/(m^2·d) (e.g., 1.7 ±0.4 mil/y) at T = 23°C to r_{Tc} = 2.6 ±0.6 g/(m^2·d) (e.g., 5.5 ±1.2 mil/y) at T = 90°C. This is only a small increase in comparison to glass, where the observed dissolution rate can increase by as much as two orders of magnitude with a 67°C increase in temperature.

A comparison of the metal corrosion rates for Amasteel and ES-32B metal phase illustrates that, at T = 90°C and pH(23°C) = 7.0, the rates are approximately the same r_{Fe} = 12.2 ± 2.7 g/(m^2·d) (e.g., 22.7 ± 5.0 mil/y) for Amasteel and r_{Fe} = 8.6 ± 1.5 g/(m^2·d) (e.g., 18.3 ± 4.0 mil/y) at T = 90°C for ES-32B metal. These results suggest that at every pH, except for the measured rate at pH(23°C) = 10.0 (pH = 8.5 at 90°C) in the absence of added O_2, the ES-32B metal and Amasteel corrode at the same rate, evident by the Fe dissolution rate being the same within the experimental error (Figure 5-7). Currently, it is unclear why the rates at pH(23°C) = 10.0 in the absence of oxygen are different for Amasteel and the ES-32B metal. Three plausible explanations for this difference in rate are (1) the formation of aqueous Fe-PO_4^{3-} complexes, (2) the formation of Fe and PO_4^{3-} surface complexes (Stumm 1997), and (3) the increase in dissolution rate caused by PO_4^{3-} being present in the aqueous solution after being released from the ES-32B metal. The complexation of Fe with PO_4^{3-} alters the Fe solution speciation and decreases the percentage of iron hydroxide complexes. This can affect the dissolution behavior of the metal by decreasing the amount of O_2 required to react with aqueous Fe(II). Similarly, the

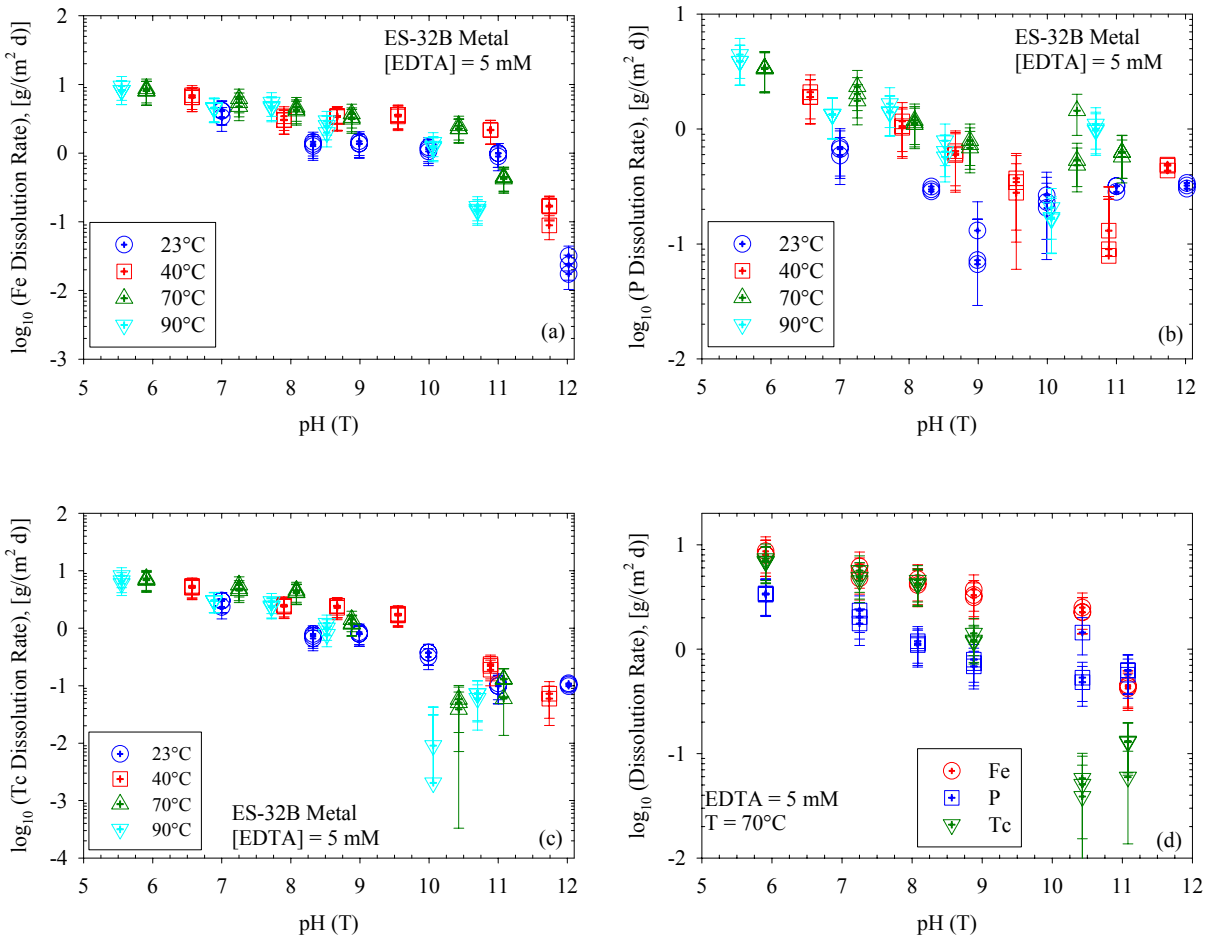

Figure 5-6. ES-32B Dissolution Rate at Each Temperature as a Function pH for Fe (a), P (b), and ^{99}Tc (c). Dissolution Rate as a Function of pH at T = 70°C for Fe, P, and ^{99}Tc (d).

exchange of PO_4^{3-} ions for OH^- ions may decrease the amount of O_2 required for the dissolution reaction to proceed, because PO_4^{3-} may decrease the number of active sites available to react in the process (Stumm 1997). An alternative explanation is that the presence of PO_4^{3-} in solution increases the dissolution rate. This increase in rate has been observed in experiments with certain Fe oxides, for example, there is a five-fold increase in the rate of Fe release from γ-Fe_2O_3 (maghemite) in a solution that contains EDTA and PO_4^{3-} (8.3 µmol/d) in comparison to solution that only contains EDTA (1.6 µmol/d) at pH(23°C) = 5.0 (Borggaard 1991). This increase in Fe release was attributed to an increase in the release rate of the Fe-EDTA complex caused by the suppression of the EDTA tetra-nuclear surface complex that forms on iron oxides by PO_4^{3-} (Borggaard 1991). Similar results were obtained for α-FeOOH, Fe_2O_3, and γ-FeOOH. Unlike the other iron minerals, the release of Fe from ferrihydrite decreased by an order of magnitude with the addition of PO_4^{3-}, from 4.2×10^3 µmol/d with EDTA to 4.6×10^2 µmol/d with EDTA and PO_4^{3-}, and this difference was attributed to differences in the crystallinity of ferrihydrite [$Fe(OH)_3$]and the other iron oxides. In either case the results provided in this report cannot fully explain the observed difference in the rates for Amasteel and ES-32B metal at pH(23°C) = 10.0 and 90°C.

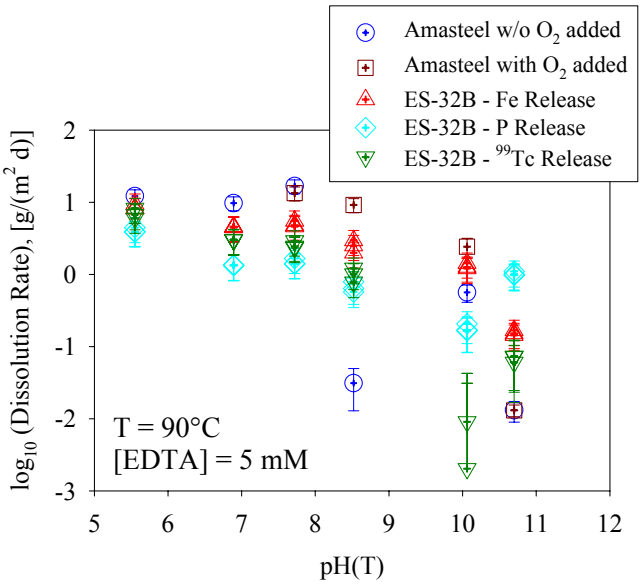

Figure 5-7. Comparison of Dissolution Rates as a Function of pH for the Low-carbon Steel and ES-32B Samples.

Based on the observed low temperature and pH dependence of the corrosion rate, we were unable to determine accurate rate-law parameters in Equation (7) for the metal. Our results indicate small temperature effects (E_a = 15 ±5 kJ/mol at pH(23°C) = 9.0 based on Fe release from ES-32B metal) and pH effects (η = -0.13 ±0.02 at 70°C based on Fe release from ES-32B metal).

5.2 STORM Simulation Results

Assuming a metal inclusion diameter of 0.5 mm, similar in size to the metal droplet shown in Hrma et al. (2005), a metal corrosion rate equal to 0.2 mil/year (1.6×10^{-13} m/s), equal to the low end of corrosion rates in Hanford soils (Table 3-1), and a mass ratio of metal to glass of 0.48% as observed in Test ES-32B (AMEC 2005), the peak flux from the metal inclusions is 3.5 My^{-1}, occurring at 730 years after the IDF is breached (Figure 5-8). This is 12.5% lower than the peak

Tc flux from 0.3% soluble salt, 4 My^{-1}, and 50 times greater than the peak Tc flux from the glass, 0.07 My^{-1}. These results show that the ^{99}Tc released from 0.5 mm metal particles in the glass is approximately the same as that released from the Tc-bearing salt.

A 0.6 mm metal droplet is shown in Hrma et al. (2005), but the average size of the metal inclusions from Test ES-32B is uncertain. To deal with this uncertainty, a range of metal inclusion diameters from 0.1 mm to 8 mm was used (Figure 5-9). Each doubling of the metal inclusion diameter results in a doubling of the peak ^{99}Tc flux from the metal inclusions, because the larger the radius of the metal inclusions, the more likely an inclusion is exposed by a fracture in the glass (Table 4-14).

A wide range of iron corrosion rates have been observed in the field (Table 3-1). To account for uncertainty in the corrosion rate of the metal inclusions, a range of corrosion rates between 1.2 μm/y (0.05 mil/y) and 20 μm/y (0.8 mil/y) were simulated for metal inclusions 2 mm in diameter. At these rates, the corrosion time for the metal inclusions exposed by fractures in the glass is short (50 to 800 years) relative to travel times through the vadose zone; the peak ^{99}Tc flux due to the metal inclusions decreases only slightly (Figure 5-10).

The amount of metallic iron that may be present in the production-scale waste packages may not be the same amount as found in the smaller packages used in Test ES-32B. To account for uncertainty in the amount of metallic iron present in the glass, various amounts of metal in the glass, from 0.12% to 1.92% by mass, were simulated for metal inclusions 2 mm in diameter, at a metal corrosion rate of 5 μm/y (0.2 mil/y) (Figure 5-11). Because the corrosion time for metal inclusions exposed by fractures in the glass is short (200 years) relative to travel times through the vadose zone, the peak ^{99}Tc flux due to the metal inclusions doubles with each doubling of metal in the waste package.

As discussed in Section 3.1, concentrations of pertechnetate as low as 5 ppm (5.05×10^{-5} mol/kg) in water have been observed to essentially stop the corrosion of iron (Cartledge 1963; Cartledge 1973). Based on simulations predicting release of Tc from a BV waste form with glass containing 0.1% Tc by weight and 0.3% soluble salt at a recharge rate of 0.9 mm/y and the underlying assumptions, Tc concentrations are likely to exceed 0.5 ppm (5×10^{-6}) mol/kg after 20 years and are likely to exceed 5 ppm between 50 and 500 years (Figure 5-8). However, after 1000 years, the Tc concentrations in most of the waste area fall below 5 ppm. Technetium released from the salt as pertechnetate and from the metal after being oxidized may increase the concentration of Tc in the leachate to the point that the corrosion of metal is inhibited during the first 500 years. However, as the Tc from the salt passes through the source area, the concentrations of Tc in the leachate would fall to the point that metal corrosion rate would gradually increase. The effect of this potential behavior would be to distribute the Tc release over many more years and decrease the peak release shown in Figure 5-8. If this potential impact was thought to be important, additional studies would be necessary to verify that the range of Tc

leachate concentrations are sufficient to stop corrosion of Fe in the Hanford disposal environment. However, delaying the release of Tc in the metal by 500 years is unlikely to have a significant impact on final groundwater concentrations.

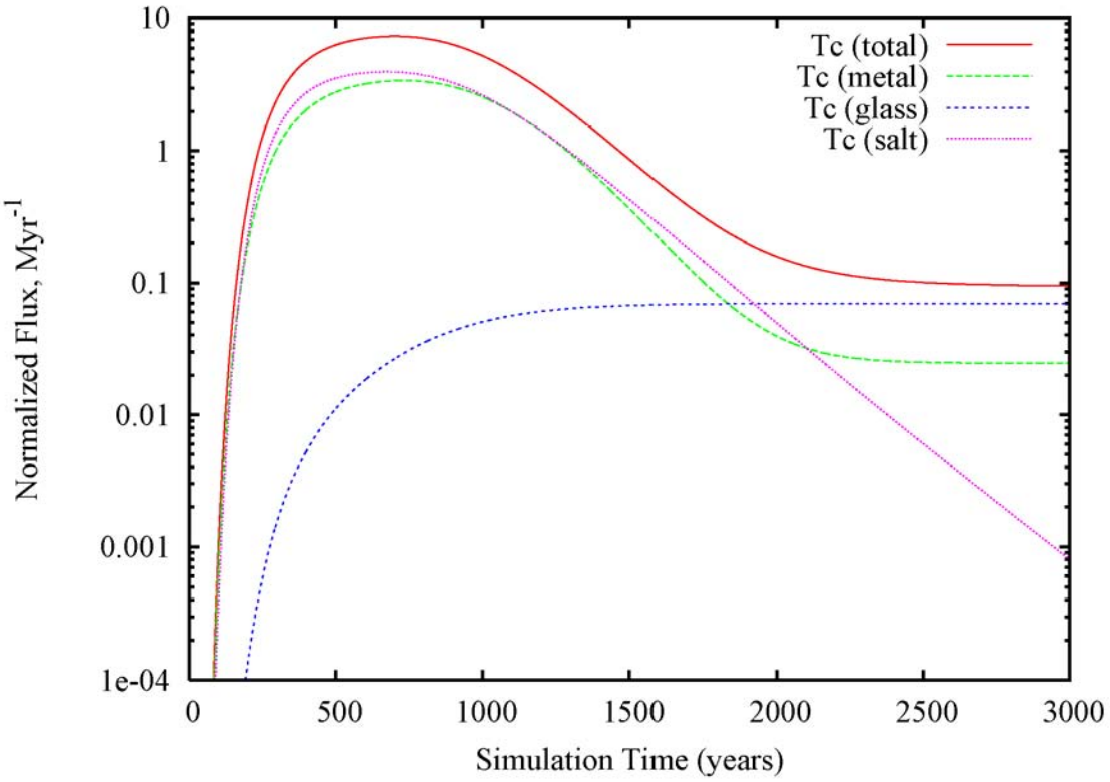

Figure 5-8. Technetium Flux to the Vadose Zone, Normalized by Total Amount of ^{99}Tc Originally in BV Waste Packages, at a Recharge Rate of 0.9 mm/y, for Metal Inclusions 0.5 mm in Diameter

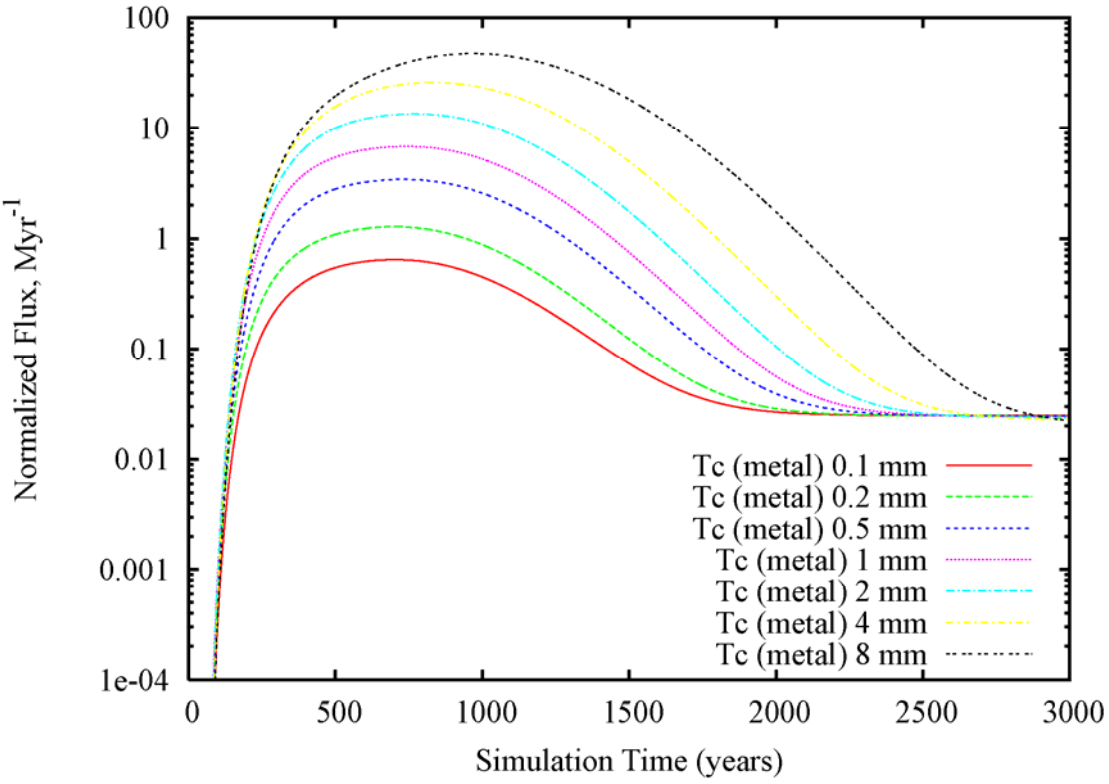

Figure 5-9. Comparison of ^{99}Tc Flux to the Vadose Zone for Various Sizes of Metal Inclusions, at a Metal Corrosion Rate of 0.2 mil/y

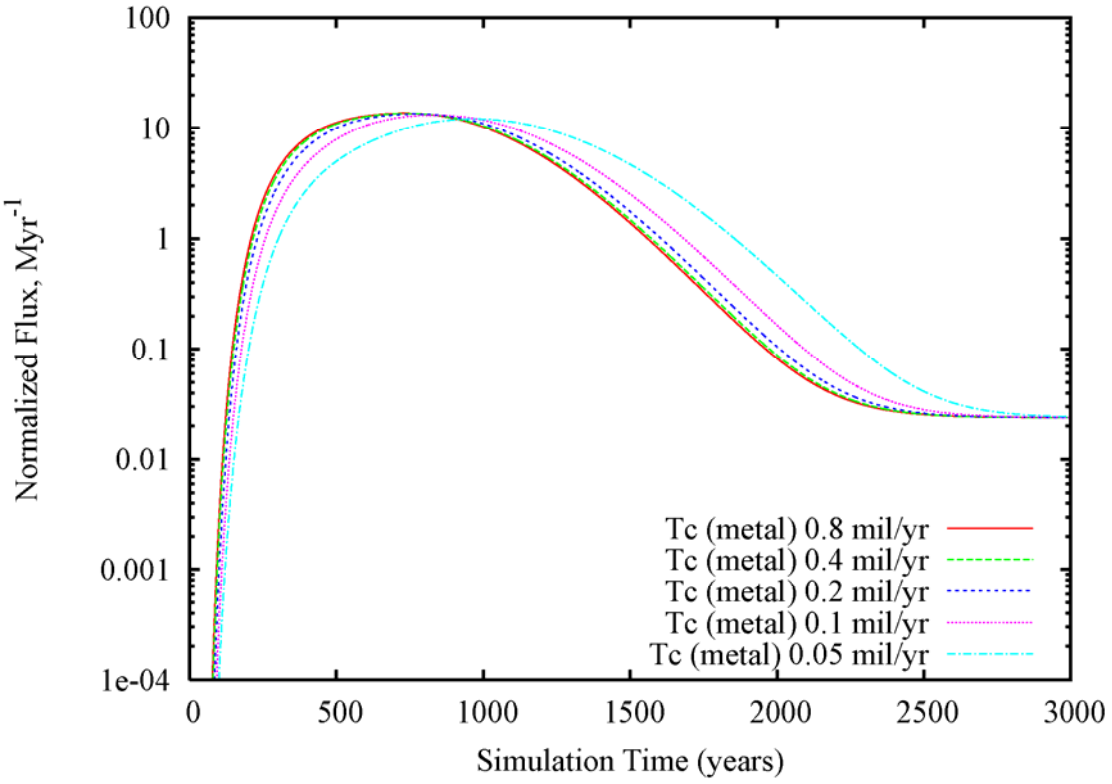

Figure 5-10. Comparison of ^{99}Tc Flux to the Vadose Zone for Various Rates of Metal Corrosion, for Metal Inclusions 2 mm in Diameter

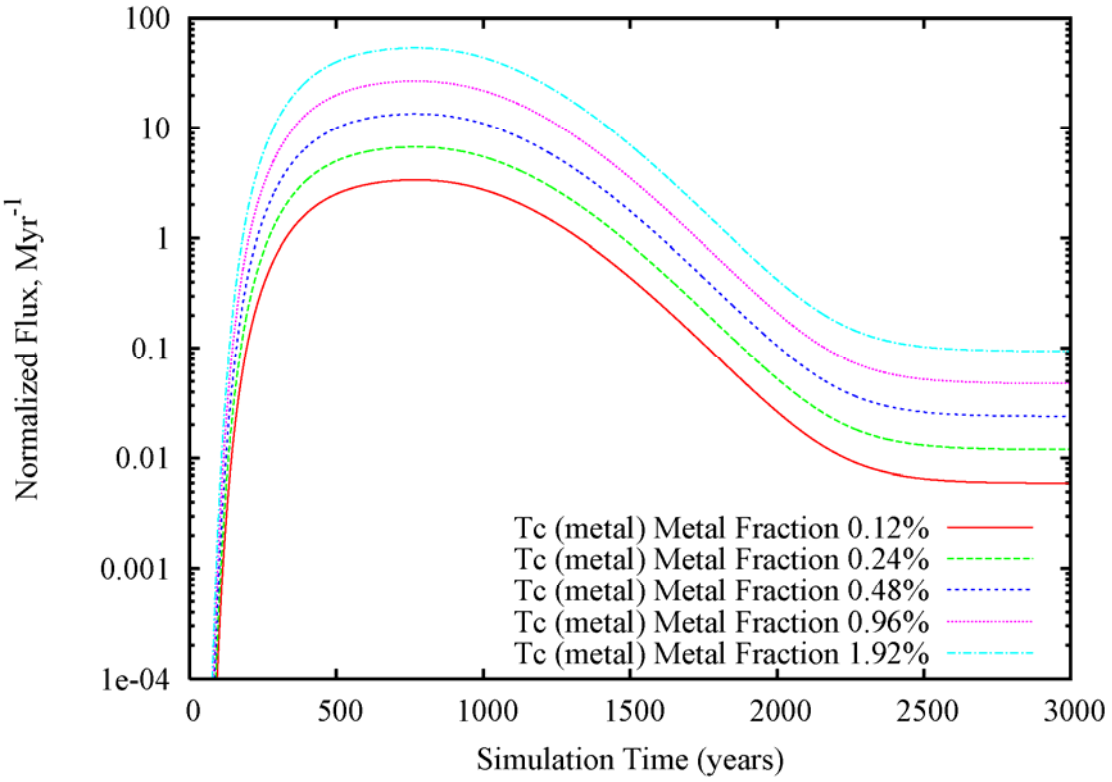

Figure 5-11. Comparison of ^{99}Tc Flux to the Vadose Zone for Various Mass Ratios of Metal to Glass, for Metal Inclusions 2 mm in Diameter, at a Metal Corrosion Rate of 50 µm/y (0.2 mil/y)

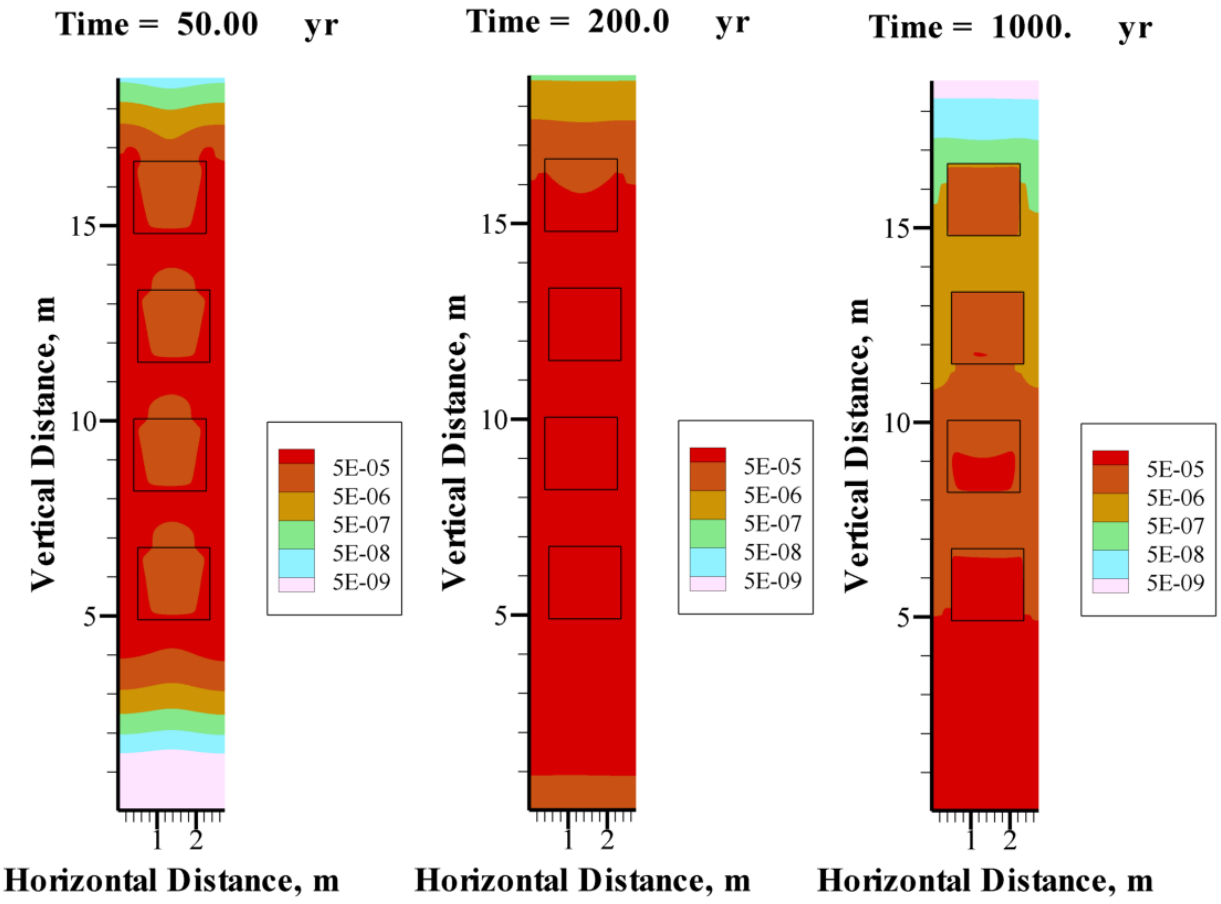

Figure 5-12. Comparison of ^{99}Tc Concentrations Surrounding BV Waste Packages at Various Times Following Emplacement

6.0 Conclusions

The dissolution kinetics of Fe(0) was quantified under conditions of constant dissolved O_2 (O_2 (aq)) and in solutions that minimized the formation of a passive film on the metal surface. The SPFT tests were conducted with EDTA solutions with pH(23°C) values in the range of 7.0–2.0, and temperatures from 23°C to 90°C. The presence of EDTA minimized the formation of a passive film and Fe-bearing secondary phases(s) during most of the testing allowing us to determine the forward dissolution rate. These results indicate the corrosion of Fe(0) is relatively insensitive to pH and temperature and the forward rate is 3 to 4 orders of magnitude higher than when a passive film and corrosion products are present. The observed decrease in rate at pH(23°C) values greater than 10.0 is probably the result of changes in the aqueous chemistry of EDTA and the Fe(III) complexes. Since no precipitates were seen on the solids from tests at these pH values, we have to conclude that some change in the concentration of the rate-limiting species was occurring or a different reaction was rate-limiting. Although the composition of the Amasteel (low carbon steel) and ES-32B metal was different, test results indicate the forward dissolution rates for both metals were similar, if not identical. In other words, the presence of minor amounts of P and ^{99}Tc in the ES-32B metal appeared to have relatively little effect on the forward rate of dissolution. These results indicate that the corrosion of the ES-32B metal at repository relevant conditions was not significantly less than the surrogate metal. Because of the small effects of temperature (E_a = 15 ±5 kJ/mol at pH(23°C) = 9.0 based on Fe release from ES-32B metal) and solution pH (η = -0.13 ±0.02 at 70°C based on Fe release from ES-32B metal), we were unable to determine accurate rate-law parameters for the metal. These forward dissolution rates were found to be very high such that under all possible repository conditions the rate would be controlled by the formation of a passivation layer and Fe(III) hydroxides and oxyhydroxides. Therefore, a corrosion rate for low carbon steel of 0.2 mil/y [0.11 g/(m^2·d)] that was determined from field tests was used for PA calculations. This corrosion rate was measured by burying weighed coupons for one year in Hanford soil under conditions similar to those expected in the IDF. Our tests showed that the dissolution rates of Amasteel and the ES-32B metal were the same within experimental error.

The results of reactive transport simulations indicate that release rates of ^{99}Tc from metal inclusions in BV waste packages emplaced in the IDF are likely to be two to four orders of magnitude higher than release rates of ^{99}Tc from the glass itself, during the first 2000 years after the IDF is breached. Release rates of ^{99}Tc from metal inclusions in BV waste packages emplaced in the IDF are insensitive to the corrosion rates assumed for the metal inclusions because the corrosion rates are fast relative to travel times through the vadose zone. Technetium-99 release rates from metal inclusions are sensitive to the size assumed for the inclusions because the larger the radius of the metal inclusions, the more likely inclusions are to be exposed by a fracture in the glass. Based on the modeling studies, peak ^{99}Tc release rates from the metal inclusions are linearly proportional to the amount of metal in the glass waste packages, whereas long-term ^{99}Tc release rates from the metal inclusions are limited by the

corrosion rate of glass. Elevated Tc concentrations due to glass corrosion may inhibit iron corrosion for 500 years, thus delaying the release of Tc from the metal. However, delaying the release of Tc in the metal by 500 years is unlikely to have a significant impact on final groundwater concentrations.

To summarize, the release of ^{99}Tc from the BV glass with precipitated Fe is directly proportional to the diameter of the particles and to the amount of precipitated Fe. However, the main contribution to the release is over the same time period as the release of the soluble Tc salt. For the base case used in this study (0.48 mass% of 0.5 mm diameter metal particles homogeneously distributed in the BV glass), the release of ^{99}Tc from the metal is approximately the same as the release from 0.3 mass% soluble Tc salt in the castable refractory block and it is released over the same time period as the salt. Therefore, to limit the impact of precipitated Fe on the release of ^{99}Tc, both the amount of precipitated Fe in the BV glass and the diameter of these particles should be minimized.

7.0 References

"Radioactive Waste Management," DOE O 435.1, U.S. Department of Energy, Washington, D.C., July 9, 1999.

Åagaard P and HC Helgeson. 1982. "Thermodynamic and Kinetic Constraints on Reaction Rates among Minerals and Aqueous Solutions. I. Theoretical Considerations." American Journal of Science, 282:237-285.

Abdelouas A, W Lutze, HE Nuttall, and WL Gong. 1999. "Remediation of U(VI)-contaminated water using zero-valent iron." Comptes Rendus De L Academie Des Sciences Serie II Fascicule A-Sciences De La Terre et Des Planetes, 328(5):315-319.

AMEC. 2005. Engineering-Scale Quantitative Test Report, Test ES-32B Final Report. 35004-RT-0001, Rev. 1, AMEC Earth & Environmental, Inc., GeoMeltTM Division, Richland, Washington.

ASTM. 2001. Standard Test Methods for Sieve Analysis of Fine and Coarse Aggregates. ASTM C136, American Society for Testing and Materials, Philadelphia, PA.

Banal N and R Doremus. 1986. Handbook of Glass Properties. Academic Press, New York.

Bacon DH and BP McGrail. 1998. "Source Term Analysis for Hanford Low-Activity Tank Waste Using the Storm Code: A Coupled Unsaturated Flow and Reactive Transport Model." In Science and Technology for Disposal of Radioactive Tank Wastes, NJ Lombardo and WW Schulz, 525, Plenum Press, Las Vegas, Nevada.

Bacon DH and BP McGrail. 2001. Waste Form Release Calculations for the 2001 Immobilized Low-Activity Waste Performance Assessment. PNNL-13369, Pacific Northwest National Laboratory, Richland, Washington.

Bacon DH and BP McGrail. 2003a. "Lessons Learned From Reactive Transport Modeling of a Low-Activity Waste Glass Disposal System." Computers and Geosciences, 29(3):361-370.

Bacon DH and BP McGrail. 2003b. "Waste Form Release Calculations for Performance Assessment of the Hanford Immobilized Low-Activity Waste Disposal Facility Using a Parallel, Coupled Unsaturated Flow and Reactive Transport Simulator." In 2002 Materials Research Society Fall Meeting Proceedings, Symposium II, Scientific Basis for Nuclear Waste Management XXVI, RJ Finch and DB Bullen, Materials Research Society, Warrendale, Pennsylvania.

Bacon DH and BP McGrail. 2005. Waste Form Release Calculations for the 2005 Integrated Disposal Facility Performance Assessment. PNNL-15198, Pacific Northwest National Laboratory, Richland, Washington.

Bacon DH, BP McGrail, VL Freedman, G Ventura, P Risoluti, and KM Krupka. 2002. "Performance Assessment of Low-Level Waste Disposal Facilities Using Coupled Unsaturated Flow and Reactive

Transport Simulators." In 2001 Materials Research Society Fall Meeting Proceedings, Symposium JJ, Scientific Basis for Nuclear Waste Management XXV, BP McGrail and GA Cragnolino, Materials Research Society, Warrendale, Pennsylvania.

Bacon DH, MD White, and BP McGrail. 2004. Subsurface Transport Over Reactive Multiphases (STORM): A Parallel, Coupled, Nonisothermal Multiphase Flow, Reactive Transport, and Porous Medium Alteration Simulator, Version 3.0, User's Guide. PNNL-14783, Pacific Northwest National Laboratory, Richland, Washington.

Ballesteros MC, EH Rueda, and MA Blesa. 1998. "The Influence of Iron (II) and (III) on the Kinetics of Geothite Dissolution by EDTA." Journal of Colloid and Interface Science, 201:13-19.

Bear J. 1979. Hydraulics of Groundwater. McGraw-Hill, New York.

Blesa MA, EB Borghi, AJG Maroto, and AE Regazzoni. 1984. "Adsorption of EDTA and Iron EDTA Complexes on Magnetite and the Mechanism of Dissolution of Magnetite by EDTA." Journal of Colloid and Interface Science, 98(2):295-305.

Bondietti G, J Sinniger, and W Stumm. 1993. "The Reactivity of Fe(III) hydroxides: Effect of Ligands in Inhibiting the Dissolution." Colloids and Surfaces A-Physicochemical and Engineering Aspects, 79:157-167.

Borggaard OK. 1991. "Iron oxide dissolution in EDTA and Oxalate." Clays and Clay Minerals, 39(3):324-328.

Bruno J, W Stumm, P Wersin, and F Brandberg. 1992. "On the influence of Carbonate in Mineral Dissolution. 1. The Thermodynamics and Kinetics of Hematite Dissolution in Bicarbonate solutions at T = 25°C." Geochimica et Cosmochimica Acta, 56(3):1139-1147.

Büchler M, P Schmuki, and H Böhni. 1997. "Formation and Dissolution of the Passive Film on Iron Studied by a Light Reflectance Technique." Journal of the Electrochemical Society, 144(7):2307-2312.

Cantrell KJ, DI Kaplan, and TW Wietsma. 1995. "Zero-Valent Iron for the In Situ Remediation of Selected Metals in Groundwater." Journal of Hazardous Materials, 42:201-212.

Cartledge GH. 1962. "Radioisotopes in the Physical Chemistry of Corrosion Processes and Their Inhibition." In RadioIsotopes in the Physical Sciences and Industry VIII, International Atomic Energy Agency, Vienna, Austria.

Cartledge GH. 1963. "Inhibition of corrosion by the pertechnetate ion." Isotopes and Radiation Technology, 1(2).

Cartledge GH. 1966. "The Passivation of Iron in the Presence of Pertechnetate and Chromate Ions." Journal of the Electrochemical Society, 4(April).

Cartledge GH. 1973. "Twenty-Year Inhibition of Corrosion by the Pertechnetate Ion." Corrosion 29(9).

Chang H-C and E Matijevic. 1983. "Interactions of Metal Hydrous Oxides with Chelating Agents IV. Dissolution of Hematite." Journal of Colloid and Interface Science, 92(2):479-488.

Chen Y, BP McGrail, and DW Engel. 1997. "Source-term analysis for Hanford low-activity tank waste using the reaction-transport code AREST-CT." Scientific Basis for Nuclear Waste Management XX, Pittsburgh.

Daveler SA and TJ Wolery. 1992. EQPT, A Data File Preprocessor for the EQ3/6 Software Package: User's Guide and Related Documentation (Version 7.0). UCRL-MA-110662 PT II, Lawrence Livermore National Laboratory, Livermore, California.

Davenport AJ, LJ Oblonsky, MP Ryan, and MF Toney. 2000. "The Structure of the Passive Film That Forms on Iron in Aqueous Environments." Journal of the Electrochemical Society, 147(6):2162-2173.

Duncan DR and LR Bunnell. 1995. Measurements of the Corrosion of Low-Carbon Steel Drums Under Environmental Conditions at Hanford: One-Year Test Results. WHC-EP-0859, Westinghouse Hanford Co., Richland, Washington.

Duncan DR, JA Demiter, and DC DeRosa. 1995. Degradation of Transuranic Waste Drums in Underground Storage at the Hanford Site. WHC-SA-3019-S, Westinghouse Hanford Co., Richland, Washington.

Farnsworth RK, MKW Chan, and SC Slate. 1985. "The Effect of Radial Temperature Gradients on Glass Fracture in Simulated High-Level Waste Canisters." Mat. Res. Soc. Symp. Proc., 44:831-838.

Fruchter JS. 2002. "In Situ Treatment of Chromium-Contaminated Groundwater." Environmental Science and Technology, 36(23):465-472.

Gambardella F, IJ Ganzevald, JGM Winkelman, and EJ Heeres. 2005. "Kinetics of the Reaction of Fe(II)-EDTA with Oxygen in Aqueous Solutions." Industrial & Engineering Chemistry Research, 44:8190-8198.

Gu B, L Liang, MJ Dickey, X Yin, and S Dai. 1998. "Reductive Precipitation of Uranium (VI) by Zero-Valent Iron." Environmental Science and Technology, 32(21):3366-3373.

Hall C and WD Hoff. 2002. Water transport in brick, stone, and concrete. Spon Press, New York.

Hrma PR, LM Bagaasen, AE Beck, TM Brouns, DD Caldwell, ML Elliott, J Matyas, K Minister, MJ Schweiger, DM Strachan, BP Tinsley, and GW Hollenberg. 2005. Bulk Vitrification Castable Refractory Block Protection Study. PNNL-15193, Pacific Northwest National Laboratory, Richland, Washington.

Khaleel R. 2004. Far-Field Hydrology Data Package for the Integrated Disposal Facility Performance Assessment. RPP-20621, Rev. 0, CH2M Hill Hanford Group, Richland, Washington.

Klausen J, PJ Vikesland, T Kohn, WP Ball, and AL Roberts. 2003. "Longevity of Granular Iron in Groundwater Treatment Processes: Solution Composition Effects on Reduction of Organohalides and Nitroaromatic Compounds." Environmental Science and Technology, 37(6):1208-1218.

Krupka KM, RJ Serne, and DI Kaplan. 2004. Geochemical Data Package for the 2005 Hanford Integrated Disposal Facility Performance Assessment. PNNL-13037 Rev. 2, Pacific Northwest National Laboratory, Richland, Washington.

Lindsay WL. 1979. Chemical Equilibria in Soils. John Wiley and Sons, New York, New York.

Lui J and D Macdonald. 2001. "The passivity of Iron in the Presence of Ethylenediaminetetraacetic Acid." Journal of the Electrochemical Society, 148(11):B425-B430.

Mann FM, KC Burgard, WR Root, RJP II, SH Finfrock, R Khaleel, DH Bacon, EJ Freeman, BP McGrail, SK Wurstner, and PE Lamont. 2001. Hanford Immobilized Low-Activity Waste Performance Assessment: 2001 Version. DOE/ORP-2000-24 Rev. 0, Department of Energy, Office of River Protection, Richland, Washington.

Mann FM, RJ Puigh, II, CR Eiholzer, Y Chen, NW Kline, AH Lu, BP McGrail, PD Rittmann, GF Williamson, NR Brown, and PE LaMont. 1998. Hanford Immobilized Low Activity Tank Waste Performance Assessment. DOE/RL-97-69 Rev. B, Project Hanford Management Contractor, Richland, Washington.

Matsushima I. 2000. "Carbon Steel--Corrosion by Soils." In Uhlig's Corrosion Handbook, RW Revie, 555-560, John Wiley & Sons.

McGrail BP, DH Bacon, WL Ebert, and KP Saripalli. 2000. A Strategy to Conduct an Analysis of the Long-Term Performance of Low-Activity Waste Glass in a Shallow Subsurface Disposal System at Hanford. PNNL-11834 Rev.1, Pacific Northwest National Laboratory, Richland, WA.

McGrail BP, DH Bacon, JP Icenhower, WL Ebert, PF Martin, HT Schaef, and EA Rodriguez. 2001. Waste Form Release Data Package for the 2001 Immobilized Low-Activity Waste Performance Assessment. PNNL-13043, Rev. 2, Pacific Northwest National Laboratory, Richland, Washington.

McGrail BP, DH Bacon, RJ Serne, and EM Pierce. 2003a. A Strategy to Assess Performance of Selected Low-Activity Waste Forms in an Integrated Disposal Facility. PNNL-14362, Pacific Northwest National Laboratory, Richland, Washington.

McGrail BP, WL Ebert, AJ Bakel, and DK Peeler. 1997. "Measurement of kinetic rate law parameters on a Na-Ca-Al borosilicate glass for low-activity waste." Journal of Nuclear Materials, 249:175-189.

McGrail BP and KM Olson. 1992. Evaluating Long-Term Performance of In Situ Vitrified Waste Forms: Methodology and Results. PNL-8358, UC-602, Pacific Northwest Laboratory, Richland, Washington.

McGrail BP, EM Pierce, HT Schaef, EA Rodriguez, JL Steele, AT Owen, and DW Wellman. 2003b. Laboratory Testing of Bulk Vitrified and Steam Reformed Low-Activity Waste Forms to Support A

Preliminary Risk Assessment for an Integrated Disposal Facility. PNNL-14414, Pacific Northwest National Laboratory, Richland, WA.

Meyer PD, KP Saripalli, and VL Freedman. 2004. Near-Field Hydrology Data Package for the Integrated Disposal Facility 2005 Performance Assessment. PNNL-14700, Pacific Northwest National Laboratory, Richland, Washington.

Meyer PD and RJ Serne. 1999. Near Field Hydrology Data Package for the Immobilized Low-Activity Waste 2001 Performance Assessment. PNNL-13035, Richland, Washington.

Mualem Y. 1976. A Catalogue of the Hydraulic Properties of Unsaturated Soils. Research Project 442, Technion, Israel Institute of Technology, Haifa, Israel.

Noradoun CE and IF Cheng. 2005. "EDTA Degradation Induced by Oxygen Activation in a Zerovalent Iron/Air/Water System." Environmental Science and Technology, 39(18):7158-7163.

Norwack B. 2002. "Environmental Chemistry of Aminopolycarboxylate Chelating Agents." Environmental Science and Technology, 36:4009.

Nowack B and L Sigg. 1996. "Adsorption of EDTA and Metal-EDTA Complexes onto Goethite." Journal of Colloid and Interface Science, 177:106-121.

Nowack B and L Sigg. 1997. "Dissolution of Fe(III) hydroxides by Metal-EDTA Complexes." Geochimica Cosmochimica Acta, 61(5):951-963.

Perry RH and DW Green. 1984. Perry's Chemical Engineer's Handbook, McGraw-Hill Book Company, New York.

Peters RD and SC Slate. 1981. "Fracturing of Simulated High-Level Waste Canisters." Nuc. Eng. Design, 67:425-445.

Pierce EM, BP McGrail, LM Bagaasen, EA Rodriguez, DW Wellman, KN Geiszler, SR Baum, LR Reed, JV Crum, and HT Schaef. 2005. Laboratory Testing of Bulk Vitrified Low-Activity Waste Forms to Support the 2005 Integrated Disposal Facility Performance Assessment. PNNL-15126, Pacific Northwest National Laboratory, Richland, WA.

Pierce EM, BP McGrail, EA Rodriguez, HT Schaef, K Saripalli, RJ Serne, PF Martin, SR Baum, KN Geiszler, LR Reed, and WJ Shaw. 2004a. Waste Form Release Data Package for the 2005 Integrated Disposal Facility Performance Assessment. PNNL-14805, Pacific Northwest National Laboratory, Richland, Washington.

Pierce EM, BP McGrail, EA Rodriguez, DM Wellman, LR Reed, DH Bacon, HT Schaef, and SR Baum. 2004b. Laboratory Testing of Bulk Vitrified Low-Activity Waste Form to Support the 2005 Integrated Disposal Facility Performance Assessment. PNNL-15126, Pacific Northwest National Laboratory, Richland, Washington.

Puigh RJ. 2004. Facility Data for the Hanford Integrated Disposal Facility Performance Assessment. RPP-20691, Rev. 0, Fluor Government Group, Richland, Washington.

Robie RA, BS Hemingway, and JR Fisher. 1978. Thermodynamic Properties of Minerals and Related Substances at 298.15K and 1 Bar Pressure and at Higher Temperatures. U.S. Geological Survey Bulletin 1452, U.S. Government Printing Office, Washington, D.C.

Rubio J and E Matijevic. 1979. "Interaction of Metal Hydrous Oxides with Chelating Agents I. □-FeOOH-EDTA." Journal of Colloid and Interface Science, 68(3):408-421.

Rueda EH, RL Grassi, and MA Blesa. 1985. "Adsorption and Dissolution in the System Goethite/Aqueous EDTA." Journal of Colloid and Interface Science, 106(1):243-246.

Santana-Casiano JM, M Gonzalez-Davila, MJ Rodriguez, and FJ Millero. 2000. "The Effect of Organic Compounds in the Oxidation Kinetics of Fe(II)." Marine Chemistry, 70:211-222.

Schwertmann U and RM Taylor. 1977. "Iron Oxides." In Minerals in Soil Environments, JB Dixon, SB Weed, JA Kittrick, MH Milford, and JL White, 145-180, Soil Science Society of America.

Serne RJ, JL Conca, VL LeGore, KJ Cantrell, CW Lindenmeier, JA Campbell, JE Amonette, and MI Wood. 1993. Solid-Waste Leach Characteristics and Contaminant-Sediment Interactions. Volume 1: Batch Leach and Adsorption Tests and Sediment Characterization. PNL-8889 Vol. 1, Pacific Northwest Laboratory, Richland, Washington.

Sikora E and D Macdonald. 2000. "The Passivity of Iron in the Presence of Ethylenediaminetetraacetic Acid I. General Electrochemical Behavior." Journal of the Electrochemical Society, 147(11):4087-4092.

Stumm W. 1990. Aquatic Chemical Kinetics: Reaction Rates of Processes in Natural Waters, John Wiley & Sons, Inc., New York, NY.

Stumm W. 1992. Chemistry of the Solid-Water Interface: Processes at the Mineral-Water and Particle-Water Interface in Natural Systems. John Wiley & Sons, Inc.

Stumm W. 1997. "Reactivity at the mineral-water interface: dissolution and inhibition." Colloids and Surfaces A-Physicochemical and Engineering Aspects, 120:143-166.

Stumm W and B Sulzberger. 1992. "The cycling of iron in natural environments: Considerations based on laboratory studies of heterogeneous redox processes." Geochimica et Cosmochimica Acta, 56:3233-3257.

Sulzberger B, D Suter, C Siffert, S Banwart, and W Stumm. 1989. "Dissolution of Fe(III) (hydr)oxides in Natural Waters; Laboratory Assessment on the Kinetics Controlled by Surface Coordination." Marine Chemistry, 28:127-144.

Sunda W and S Huntsmann. 2003. "Effect of pH, Light, and Temperature on Fe-EDTA chelation and Fe Hydrolysis in Seawater." Marine Chemistry, 84:35-47.

Wehrli B, B Sulzberger, and W Stumm. 1989. "Redox Processes Catalyzed by Hydrous Oxide Surfaces." Chemical Geology, 78:167-179.

Wolery TJ. 1992. EQ3NR, A Computer Program for Geochemical Aqueous Speciation-Solubility Calculations: Theoretical Manual, User's Guide, and Related Documentation (Version 7.0). UCRL-MA-110662 PT III, Lawrence Livermore National Laboratory, Livermore, California.

Wolery TJ and SA Daveler. 1992. EQ6, A Computer Program for Reaction Path Modeling of Aqueous Geochemical Systems: Theoretical Manual, User's Guide, and Related Documentation (Version 7.0). UCRL-MA-110662 PT IV, Lawrence Livermore National Laboratory, Livermore, California.

Wolery TW and RL Jarek. 2003. Software User's Manual, EQ3/6, Version 8.0. 10813-UM-8.0-00, Sandia National Laboratories, Albuquerque, New Mexico.

Yabusaki SB, KJ Cantrell, B Sass, and CI Steefel. 2001. "Multicomponent Reactive Transport in an In-Situ Zero-Valent Iron Cell." Environmental Science and Technology, 35:1493-1503.

Zinder B, G Furrer, and W Stumm. 1986. "Coordination Chemistry of Weathering II: Dissolution of Fe(III) oxides." Geochimica Cosmochimica Acta, 50:1861-1869.

Zutic V and W Stumm. 1984. "Effect of Organic Acids and Fluoride on the Dissolution Kinetics of Hydrous □-FeOOH. A Model Study using the Rotating Disc Electrode." Geochimica Cosmochimica Acta, 48:1493-1503.

Distribution

No. of Copies

OFFSITE

3 **AMEC Earth & Environmental**

L Thompson	B2-67
K Witwer	B2-67
J Reddick	B2-67

ONSITE

4 **U.S. DOE Office of River Protection**

ME Burandt	H6-60
BM Mauss	H6-60
JF Thompson	H6-60
SA Wiegman	H6-60

10 **CH2M HILL Hanford Group, Inc.**

SC Davis (2)	S7-67
MW Leonard	S7-67
FM Mann	H6-03
FR Miera	H6-03
G Parsons	S7-67
DL Parker	H6-03
RE Raymond	S7-83
JE Van Beek (2)	S7-67

No. of Copies

ONSITE

37 **Pacific Northwest National Laboratory**

LM Bagaasen (10)	K6-28
DH Bacon (10)	K9-33
TM Brouns	K9-39
CF Brown	P7-22
ML Elliott	K6-28
GB Josephson	K9-69
PR Hrma	K6-24
D-S Kim	K6-24
KM Krupka	K6-81
EM Pierce (5)	K6-81
RJ Serne	P7-22
DM Strachan	K6-24
DM Wellman	K6-81
Hanford Technical Library (2)	P8-55